

# Recent Progress and Future Opportunities for Hot Carrier Photodetectors: From Ultraviolet to Infrared Bands

Cheng Zhang, Yu Luo, Stefan A. Maier, and Xiaofeng Li\*

The hot carriers generated from the nonradiative decay of surface plasmons in metallic nanostructures can inject into the conduction band of a semiconductor, allowing for the sub-bandgap photodetection under room temperature. By the controllable interfacial barrier height between the plasmonic and semiconductor/insulator materials, the hot carrier photodetectors working from ultraviolet to infrared bands are extensively demonstrated with significant progress. In this review, hot carrier dynamics are briefly discussed from generation, transport, and emission perspectives. The state-of-the-art progress of hot carrier photodetectors with various configurations, material constitutions, and plasmonic nanostructures are surveyed. To further promote hot carrier extraction efficiency toward the practical applications, the thermodynamic loss analysis, and the potential strategies from the optical, electrical, and material perspectives are addressed. The performances of the developed hot carrier photodetectors are also summarized, particularly addressing the novel functionalities, challenges, and future opportunities.

relieve the parasitic loss in metals.<sup>[7]</sup> Generally, SPs can decay radiatively into the reemitted photons or nonradiatively into the energetic carriers (i.e., hot electrons and hot holes in metals) via the intraband or interband transitions.<sup>[8]</sup> Hot carriers are further thermalized by electron–electron scattering in tens of femtoseconds and cooled via transferring the energy to the lattice as the heat via electron–phonon scattering in picoseconds.<sup>[9]</sup> Therefore, the nonradiative decay of SPs usually leads to severe parasitic heat loss and limits the performance of plasmonic devices.<sup>[10]</sup> For example, in some cases, the existing parasitic absorptions in plasmonic solar cells prevent the achievement of satisfactory photocurrent enhancement.<sup>[11]</sup>

Recently, the direct utilization of hot carriers in metals has been proposed as a promising strategy in photothermal photodetectors, photovoltaics, and photocatalysis.<sup>[12–18]</sup> For instance, the localized photothermal heating of the metallic nanoparticles adhered to tumor under the illumination of resonant light can kill tumor cells; the injection of hot carriers into a semiconductor or molecules at the surface is expected to realize more efficient photovoltaic and photocatalytic devices; by forming a Schottky barrier with a semiconductor,<sup>[19]</sup> hot carrier photodetectors have unique properties such as sub-bandgap photodetection, convenient fabrication, self-powered and room-temperature operation, and high tunability (e.g., bandwidth, working wavelength,

## 1. Introduction

In the past decades, the plasmonic community has experienced a flourishing because surface plasmons (SPs) promise huge potential for boosting the performances for a large number of applications, such as sub-wavelength lens,<sup>[1]</sup> photovoltaic cells,<sup>[2]</sup> photodetectors,<sup>[3]</sup> light sources,<sup>[4]</sup> and sensors.<sup>[5]</sup> The strong interaction between light and free electrons in metals provides a salient property of SPs to confine optical fields into sub-wavelength volumes.<sup>[6]</sup> However, one great challenge of employing SPs to improve the device performance lies in how to

nanotherapeutics, photodetectors, photovoltaics, and photocatalysis.<sup>[12–18]</sup> For instance, the localized photothermal heating of the metallic nanoparticles adhered to tumor under the illumination of resonant light can kill tumor cells; the injection of hot carriers into a semiconductor or molecules at the surface is expected to realize more efficient photovoltaic and photocatalytic devices; by forming a Schottky barrier with a semiconductor,<sup>[19]</sup> hot carrier photodetectors have unique properties such as sub-bandgap photodetection, convenient fabrication, self-powered and room-temperature operation, and high tunability (e.g., bandwidth, working wavelength,

C. Zhang, X. Li  
School of Optoelectronic Science and Engineering and Collaborative  
Innovation Center of Suzhou Nano Science and Technology  
Soochow University  
Suzhou 215006, China  
E-mail: xfli@suda.edu.cn


C. Zhang, X. Li  
Key Lab of Advanced Optical Manufacturing Technologies of Jiangsu  
Province and Key Lab of Modern Optical Technologies of Education  
Ministry of China  
Soochow University  
Suzhou 215006, China

Y. Luo  
School of Electrical and Electronic Engineering  
Nanyang Technological University  
Nanyang Avenue, Singapore 639798, Singapore

S. A. Maier  
School of Physics and Astronomy  
Monash University  
Clayton Victoria 3800, Australia

S. A. Maier  
The Blakett Laboratory  
Department of Physics  
Imperial College London  
London SW7 2AZ, UK

S. A. Maier  
Chair in Hybrid Nanosystems  
Nanoinstitut München, Fakultät für Physik,  
Ludwig-Maximilians-Universität München  
München 80539, Germany

 The ORCID identification number(s) for the author(s) of this article can be found under <https://doi.org/10.1002/lpor.202100714>

DOI: 10.1002/lpor.202100714

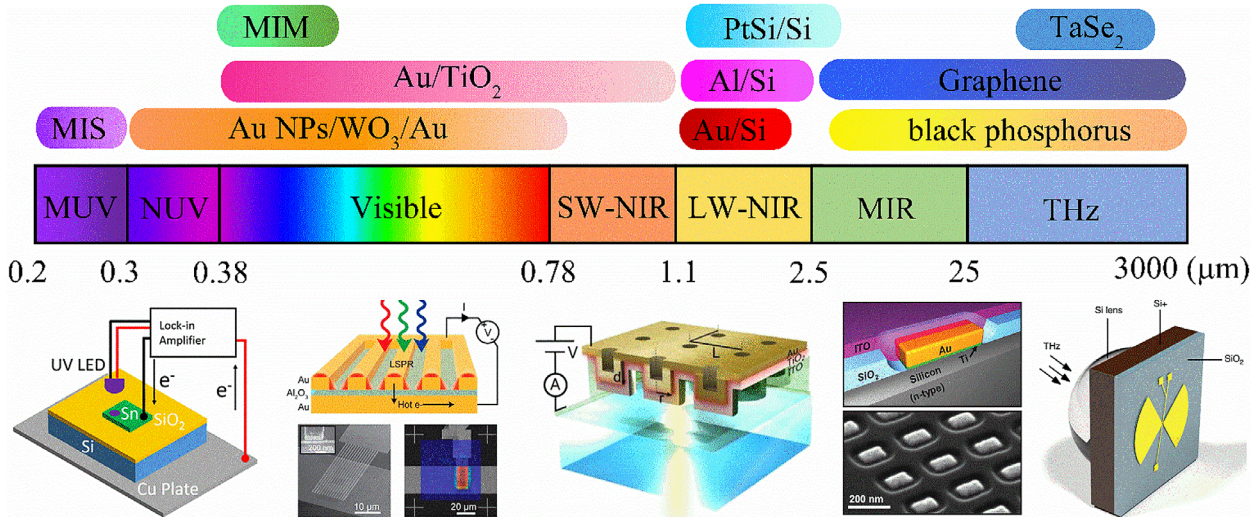


**Figure 1.** A diagram of the electromagnetic spectrum, and the different types of hot carrier photodetectors from ultraviolet to THz bands. Hot carrier photodetectors can work in a broadband wavelength range from middle ultraviolet to THz bands by modulating the interfacial barrier. Reproduced with permission.<sup>[13]</sup> Copyright 2011, American Association for the Advancement of Science. Reproduced with permission.<sup>[21]</sup> Copyright 2018, American Chemical Society. Reproduced with permission.<sup>[22]</sup> Copyright 2014, American Chemical Society. Reproduced with permission.<sup>[24]</sup> Copyright 2015, American Chemical Society. Reproduced with permission.<sup>[25]</sup> Copyright 2018, Springer Nature.

and polarization-dependence). The barrier height varies from  $\approx 3.8$  eV [e.g., stannum/silicon dioxide (Sn/SiO<sub>2</sub>)] to 0.3 eV [e.g., platinum silicide/p type-silicon (PtSi/p-Si)] depending on the materials of the junction and can be modified by the fabrication method and surface treatment.<sup>[20,21]</sup> **Figure 1** shows that hot carrier photodetectors can work in a long spectral range from the ultraviolet (UV), visible, infrared (IR) to terahertz (THz) bands as shown in the electromagnetic spectrum.<sup>[13,21–27]</sup> For example, hot electrons are utilized in the Sn–SiO<sub>2</sub>–Si system with a barrier height ( $\Phi_b$ ) of  $\approx 3.8$  eV to implement solar-blind UV detection.<sup>[21]</sup> In addition, the plasmonic stripe antenna in the gold–aluminum oxide–gold (Au–Al<sub>2</sub>O<sub>3</sub>–Au) structure ( $\Phi_b = 2.6$  eV) and the plasmonic crystals of gold–titanium dioxide–Indium tin oxide (Au–TiO<sub>2</sub>–ITO,  $\Phi_b = 0.68$  eV) are reported to improve the photoresponse across the visible and near-infrared bands by exciting surface plasmon resonances.<sup>[22,24]</sup> Based on Si, hot electrons play a role in telecommunication photodetection, potentially replacing the costly Indium gallium arsenide (InGaAs) and germanium (Ge) detectors.<sup>[13]</sup> Using graphene plasmons, the resonant THz photodetection is demonstrated by antenna-coupled graphene transistors.<sup>[25]</sup>

Despite these advantages, one key ingredient that limits the actual application of hot carrier photodetectors is the low photoconversion efficiency.<sup>[19]</sup> To promote the practical application of hot carrier photodetectors, new plasmonic and semiconductor materials, structures, mechanisms, and functionalities have been reported with significant progress. A comprehensive review investigation on the latest development of the hot carrier photodetectors working from ultraviolet to infrared bands, including hot carrier dynamics, plasmonic and planar hot carrier photodetectors, especially on the efficient strategies (e.g., structures, materials, and mechanisms) to relieve the losses and novel functionalities, is highly useful. Here we aim to provide a comprehensive review on hot carrier photodetectors, starting from the fundamentally thermodynamic analysis to the developed strate-

gies and novel functionalities in recent years. The related topics regarding the detailed hot carrier dynamics, photocatalysis, and photovoltaics can refer to the works of literature.<sup>[3,8,10,28–32]</sup> In addition, the hot carriers can also be generated in semiconductors and the relaxation dynamics are different from that in metals. Here, we focus on the fundamentals and applications of hot carriers in metals, and that in semiconductors can be found from other reviews.<sup>[33,34]</sup> In this review, Section 2 describes the nature of hot carrier photoconversion processes, involving the physics of hot carrier generation, transport, and emission processes from the theoretical and experimental perspectives. Section 3 focuses on the recent development of hot carrier photodetectors from ultraviolet to infrared with varying material constitutions and device architectures. Section 4 concentrates on the thermodynamic loss analysis for hot-carrier photoconversion processes and the experimentally reported strategies for improving the device performance from the optical, electrical, and material perspectives. A detailed analysis of the key performance parameters of hot carrier photodetectors and their novel functionalities are also introduced. Finally, we present a detailed performance comparison of the reported hot carrier photodetectors and address the potential perspectives for higher efficiencies.

## 2. Hot Carrier Dynamics and Microscopic Processes

A complete microscopic picture of hot carrier photoconversion processes involves mostly the generation, transport, and emission of hot carriers.<sup>[20]</sup> That is to say, hot carriers are generated in metals by absorbing photons, then some of them reach the Schottky interface without experiencing electron–electron scattering, and finally, those with enough energy and matched momentum are successfully injected into the conduction band of the semiconductor layer. The overall photoconversion efficiency depends on the product of all these individual efficiencies. We now

introduce the theoretical and experimental investigations on hot carrier dynamics and microscopic processes.

## 2.1. Hot Carrier Generation

The hot carrier generation rate and the initial energy/spatial/momentum distributions upon generation are the key factors to be considered in the process. There are vast theoretical investigations on this topic since the experimental studies are very challenging. Until recently, the first experimental quantification of hot carrier energy distributions is realized based on a scanning probe-based approach.<sup>[35]</sup> To obtain microscopic insight into hot carrier generation with a quantitative description of ultrafast dynamics in noble metals, density function theory, GW (for the electron self-energy calculation,  $G$  is the Green function,  $W$  is the screened Coulomb potential), and electron–phonon calculations are combined in a quantum mechanical framework to study hot carrier energy distribution and scattering processes by the excitation of surface plasmon polaritons (SPPs) in Au and silver (Ag).<sup>[36]</sup> Figure 2A shows the diagram for the study of hot carrier generation from SPPs at the metal–dielectric interface. It is found that for the intraband transition (i.e., SPP energy lower than the interband threshold), the decay of SPPs leads to high-energy hot carriers (1–2 eV above Fermi energy) with long mean free paths (MFPs) up to 40 nm, which is preferable for hot carrier extraction. While for the interband transition (i.e., SPP energy higher than the interband threshold), the decay of SPPs leads to low-energy hot electrons (<1 eV above Fermi energy) and short-lived hot holes with MFP of  $\approx 1$  nm. The first comprehensive theoretical description of the hot carrier generation process is realized in spherical silver nanoparticles and nanoshells based on the description of the conduction electrons in metal as free particles under Fermi's golden rule, as shown in Figure 2B.<sup>[37]</sup> The analysis reveals that metallic particle size and hot carrier lifetime are crucial in determining the hot carrier generation and energy distribution, i.e., the hot carrier generation rates (initial energies) are higher (lower) in larger metallic nanoparticles and carriers of shorter carrier lifetimes. In addition, hot carriers are primarily generated along the direction parallel to the polarization of the external electric field. Based on quantum linear response theory, the wave function of a plasmon in nanostructured metals of different sizes is analyzed to understand the behaviors of excited electrons in optically driven metal nanocrystals.<sup>[38]</sup> Figure 2C shows the schematics of electron transitions and the initial electron energy distribution in 10 nm gold nanocubes. The same conclusion as that in Figure 2B is obtained: the high-energy carriers are preferentially generated in small-size nanocrystals. It is noted that there is a contradiction regarding the choice of the metallic size for efficient hot carrier generation (high hot carrier generation rate or larger initial energies). To design high-performance hot carrier photodetectors, the detailed generation, transport, and collection processes of hot carriers should be considered. Recently, it is demonstrated that large-size nanocrystals contribute to an overall higher photoconversion efficiency.<sup>[39]</sup> For efficient hot carrier generation and injection, the exciting light should be polarized along the smallest dimension of a nanostructure and normal to the Schottky barrier interface.

With coupled master equations, the instantaneous hot carrier distribution as a function of time after excitation is investigated with the consideration of electron–electron, electron–photon, and electron–phonon scattering as illustrated in Figure 2D.<sup>[40]</sup> It reveals that electron–electron scattering is the dominant relaxation, where hot carrier energy is transferred to the cold carriers and leads to the multiplication of low-energy carriers. During the relaxation, a small fraction of electrons radiatively recombine with holes and emit photons. When the carrier energy is close to the Fermi level, electron–phonon scattering dominates and heats the nanoparticles. Using a quantized plasmon model with a detailed electronic structure, the prompt energy distributions of hot carriers due to interband direct transitions in several metals are studied.<sup>[41]</sup> Figure 2E shows that the initial hot carrier energy distribution is sensitive to the electronic band structure due to the selection rule for electron transition. In gold and copper, the electrons from the d-bands deep below the Fermi level are predominantly transitioned to the conduction band, leaving high-energy hot holes and generating low-energy hot electrons. While for silver and aluminum, the energy distribution is more equitable between electrons and holes. Due to the selection rule, the initial hot carrier momentum distribution is anisotropic and dominated by the plasmon polarization and the crystal orientation for aluminum and noble metals, respectively. By including *ab initio* electronic structure calculation for phonon-assisted transitions,<sup>[42]</sup> Figure 2F shows that at low frequencies, the phonon-assisted transitions generate a uniform hot carrier energy distribution from zero to plasmon energy and compete with the resistive losses. At high frequencies above the interband threshold, the direct transitions dominate and the corresponding hot carrier initial energy distribution is dependent on plasmonic metals, which is consistent with that in Figure 2E. Furthermore, the hot carrier MFPs accounting for electron–electron and electron–phonon scattering are calculated, providing further insight into the carrier transport behaviors, as discussed below.

## 2.2. Hot Carrier Transport

Upon generation, hot carriers rapidly travel through the material along the initial momentum direction, scatter against electrons, phonons, and defects, and finally reach the thermal equilibrium with the electrons at the Fermi level.<sup>[10]</sup> Hot carrier photodetection requires the carriers to have enough excess energy relative to the Fermi level to transfer across the Schottky barrier into the semiconductor conduction bands.<sup>[20]</sup> Thus, it is necessary to collect hot carriers with minimum scattering for efficient photodetection. From the experimental perspective, hot carrier transport dynamics are typically studied by the ultrafast pump-probe measurement, using a high-intensity laser pulse to excite electrons and measure the optical response with a delayed probe pulse. From the theoretical perspective, hot carrier transport in plasmonic structures can be solved using the Boltzmann equation or Monte Carlo method, which however requires large amounts of computation unless under sufficient approximates.

The hot electron momentum distribution in individual Au nanorods is investigated by a time-of-flight momentum resolving photoemission electron microscope.<sup>[43]</sup> The Au nanorods are adhered to the ITO substrate with a controlled size to have a

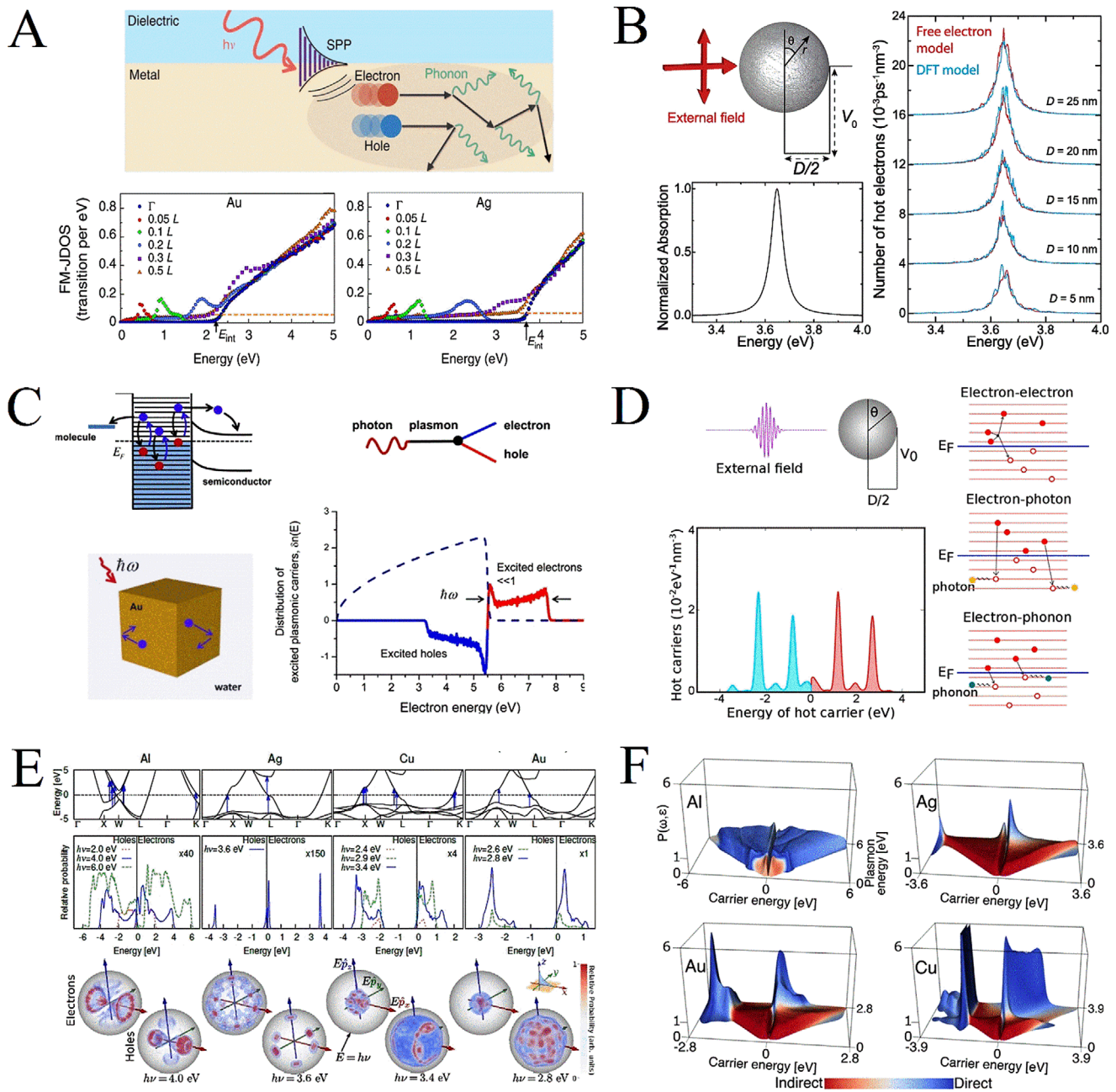


**Figure 2.** A) Top: schematic of a metal–dielectric interface under illumination. Bottom: the finite momentum joint density of states (FM-JDOS) of Au (left) and Ag (right) as a function of SPP energy for several values of crystal momentum. Reproduced with permission.<sup>[36]</sup> Copyright 2015, Springer Nature. B) Left: schematic of the system under study (top) and normalized absorption spectrum for the silver nanoparticle in the quasi-static limit (right). Right: hot electrons generation rate as a function of light frequency under various nanoparticle diameters. Reproduced with permission.<sup>[37]</sup> Copyright 2014, American Chemical Society. C) Left: schematic of the electron transition process in a metal crystal (top) and electrons bouncing off the walls in an Au nanocube. Right: illustrations of plasmonic processes within the linear-response many-body theory model (top) and the initial hot-electron energy distribution in a 10 nm gold nanocube by the excitation of localized plasmon (bottom). Reproduced with permission.<sup>[38]</sup> Copyright 2014, Elsevier Ltd. D) Left: schematic of the silver jellium nanoparticle system under study (top) and initial hot carrier energy distribution after plasmon decay in the nanoparticle system with a diameter of 6 nm. Reproduced with permission.<sup>[40]</sup> Copyright 2017, American Chemical Society. E) Top: schematic of the allowed interband transitions on the electronic band structure of aluminum (Al), Ag, copper (Cu), and Au. The initial hot carrier energy (middle) and the energy-momentum distribution (bottom) by the interband transition. Reproduced with permission.<sup>[41]</sup> Copyright 2014, Springer Nature. F) Hot carrier initial energy distributions as a function of carrier energy and plasmon frequency due to the phonon-assisted and direct transitions in Al, Ag, Au, and Cu. Reproduced with permission.<sup>[42]</sup> Copyright 2016, American Chemical Society.

plasmonic resonance at the wavelength of 800 nm (Figure 3A). The measured hot-electron momentum distribution suggests two mechanisms for electron emission: 1) main isotropic momentum distribution arising from the optical-thermally assisted multiphoton emission process and 2) a small fraction of strongly directional momentum distribution parallel to the nanorod's long axis (i.e., polarization direction) due to the near field enhancement at both nanorod tips. The fraction of directed electron momentum distribution increases with the laser peak power density and is favorable for hot electron photodetection. Based on the first-principles calculations of carrier dynamics and optical responses, Figure 3B shows that the theoretical description matches well with spectral and temporal features in pump-probe measurements.<sup>[44]</sup> By accounting for the detailed electronic band effects in the density of states, the initial hot carrier energy distribution after generation, the electron–phonon coupling, and dielectric functions, the theory allows to exactly predict hot carrier transport dynamics without using empirical parameters for both the dynamics and response of the electrons in the conventional “two-temperature model.” With femtosecond-resolution measurements, it is confirmed that the adiabatic nanofocusing surface plasmon tapers can efficiently generate hot carriers at the apex by slowing down plasmons at the taper apex, as shown in Figure 3C.<sup>[45]</sup> A substantial increase of the lifetime of the hot electron gas temperature is observed at the apex compared to the electron thermalization time and that in small Au nanoparticles, which is ascribed to the intricate heat flow at the apex from the two-temperature model analysis.

In addition, hot carrier dynamics can be described by a master equation incorporating transition rates for optical excitations and electron–electron collisions.<sup>[46]</sup> Figure 3D shows the evolution process of hot carriers in small gold and silver nanoparticles: 1) the excitation by a laser pulse, 2) the thermalization over 10 fs to the elevated electron temperatures due to electron–electron scattering, and 3) eventual relaxation in several ps to ambient temperature due to electron–phonon scattering and thermal diffusion. The temporal evolution of hot carrier energy distribution is strongly dependent on the photon energy, particle size, and pulse fluence. To capture the essential features in the complex hot carrier transport dynamics, the simplified time-dependent spatially homogeneous Boltzmann equation is solved.<sup>[10]</sup> Figure 3E shows the evolution of hot carrier energy and momentum distribution versus carrier transport distance in gold at the excitation of photons of 2.6 eV. The interband transition gives rise to strongly anisotropic high (low) energy holes (electrons), which significantly (rarely) scatter at the transport distance of  $L = 3$  nm. Hot holes have a uniform energy distribution at  $L = 10$  nm, and both hot electrons and holes are thermalized to less than 1 eV at  $L = 30$  nm. Finally, hot carriers are completely thermalized at  $L = 100$  nm with an isotropic momentum distribution. Additionally, the plasmon-assisted hot carrier dynamics in optical gold antennas are investigated by nonlinear autocorrelation measurements, as illustrated in Figure 3F.<sup>[47]</sup> The nonlinear hot electron generation efficiency can be increased 100-fold by the excitation of surface plasmon resonance. The hot carrier energy distribution is enlarged arising from the elevated electronic temperature above 1000 K. Furthermore, the temporal response of the carrier relaxation can be controlled by the light resonance and power density, within the range from 500 fs to 2.5 ps. Finally, the nonlinear ab-

sorption cross-section of the plasmonic antennas is determined by a quantitative analysis of the relaxation dynamics, providing new insights on the understanding of hot carrier generation.

### 2.3. Hot Carrier Emission

The hot carriers generated upon the excitation of surface plasmons (Figure 4A) are thermalized after scattering against other cold electrons and phonons on a timescale of picosecond and then transfer the excess energy to heat.<sup>[48]</sup> Hot carriers are normally collected by a Schottky junction formed by placing a semiconductor in contact with the metallic nanostructures, as shown in Figure 4B. The hot carriers in the vicinity of the Schottky junction have a higher probability to reach the Schottky interface and inject into semiconductors compared to those far away from the interface. The collection efficiency of hot carriers over a Schottky junction is usually described by the Fowler model.<sup>[20]</sup> Hot carriers can be injected into semiconductors if their kinetic energies from the normal components of momentum are larger than the Schottky barrier height. As a result, only those within the emission cone can be collected (Figure 4C). Recently, a hot carrier transport model based on the Monte Carlo method is proposed to investigate the hot carrier injection efficiency in nanometer-sized metal structures.<sup>[49]</sup> The hot carriers cannot inject into semiconductors after an electron–electron scattering. Since the mass of a phonon is much smaller than that of an electron, the electron–phonon scattering events can be considered as elastic and isotropic, i.e., the electron–phonon scattering only modifies the momentum direction without changing the carrier energy (Figure 4D). Based on the further assumption of isotropic momentum distribution, uniform energy, and spatial distributions upon generation in the nanoscale metals, the effect of metal size and shape on hot carrier injection efficiency is investigated. By ignoring the electron–phonon scattering, the result of the Fowler model is perfectly reproduced by the Monte Carlo method. The study shows that electron–phonon scattering is beneficial for the carrier injection process by changing the momentum directions of hot carriers that previously fail to be injected.

The efficiencies of the three-step hot carrier generation, transport, and emission processes are normally low than 1%.<sup>[50]</sup> Recently, the one-step hot-carrier transfer process called the plasmon-induced interfacial charge-transfer transition is reported to directly excite electrons from the metal to a strongly coupled semiconductor via the plasmon decay (Figure 4E).<sup>[48]</sup> Based on this mechanism, the hot carrier extraction efficiency can be up to 24%, independent of the photon energy over a 1 eV range. Figure 4F shows an alternative approach to collect hot carriers by forming a metal–insulator–metal (MIM) junction.<sup>[22]</sup> Hot carriers are generated in one metal, diffuse to the metal/insulator interface, inject into the insulator, transport across the insulator, and inject into the opposite metal. Following the similar approach of the three-step model, the hot carrier collection efficiency of the five-step process in the MIM configuration is quantified by further considering the carrier reflection at the metal/insulator interface due to the momentum mismatch in the metal and the insulator (Figure 4G). Since hot carriers can be generated in both metals, the net photocurrent is the difference between that collected by two metallic contacts.

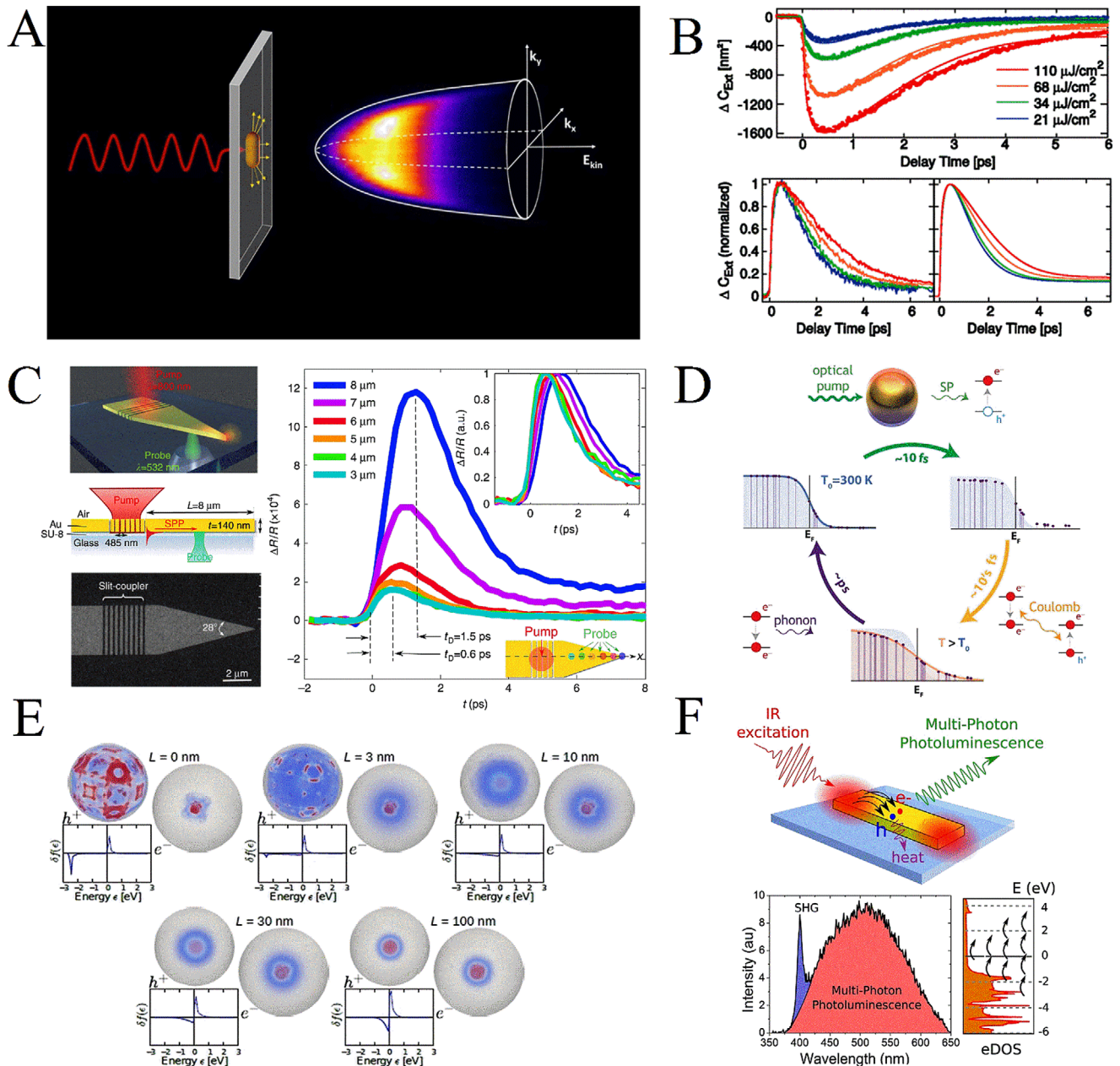


**Figure 3.** A) Schematic of the electron emission measurement experiment by femtosecond linear polarized, laser pulses from an individual Au nanorod with the 3D spectral density function of the emitted electrons shown in right. Reproduced with permission.<sup>[43]</sup> Copyright 2017, American Chemical Society. B) Top: comparison of the absolute measurements (circles) and calculated differential cross-sections (solid lines) at 530 nm probe wavelength for pump excitation at 560 nm. Bottom: measured (left) and predicted differential cross-sections over the full-time range. Reproduced with permission.<sup>[44]</sup> Copyright 2017, American Physical Society. C) Left: schematic (top), line shape (middle), and scanning electron microscope (SEM) of the plasmonic coupler-taper platform with a pump pulse focused from the air onto a slit array. Right: time-resolved hot carrier dynamics: position-dependent transient  $\Delta R/R$  signals as a function of the pump-probe delay. Reproduced with permission.<sup>[45]</sup> Copyright 2017, Springer Nature. D) Schematic of the physical processes under consideration including 1) the initially thermal equilibrium with background, 2) an ultrafast laser pulse irradiation on the particle to excite surface plasmons, which decays into hot carriers, 3) the charge carriers evolve to the most energetic electrons by Coulomb interaction and eventually relaxing back to ambient temperature via electron–phonon scattering. Reproduced with permission.<sup>[46]</sup> Copyright 2016, American Chemical Society. E) The evolution of hot carrier energy-momentum distribution as a function of transport distance  $L$  considering the electron–electron and electron–phonon scattering. Reproduced with permission.<sup>[10]</sup> Copyright 2016, De Gruyter. F) Top: schematic of the multiphoton photoluminescence due to the nonlinear plasmon-induced hot carrier generation. Bottom: typical nonlinear emission spectrum of a thin gold film (left) and the electronic density of state in Au (right). Reproduced with permission.<sup>[47]</sup> American Chemical Society.

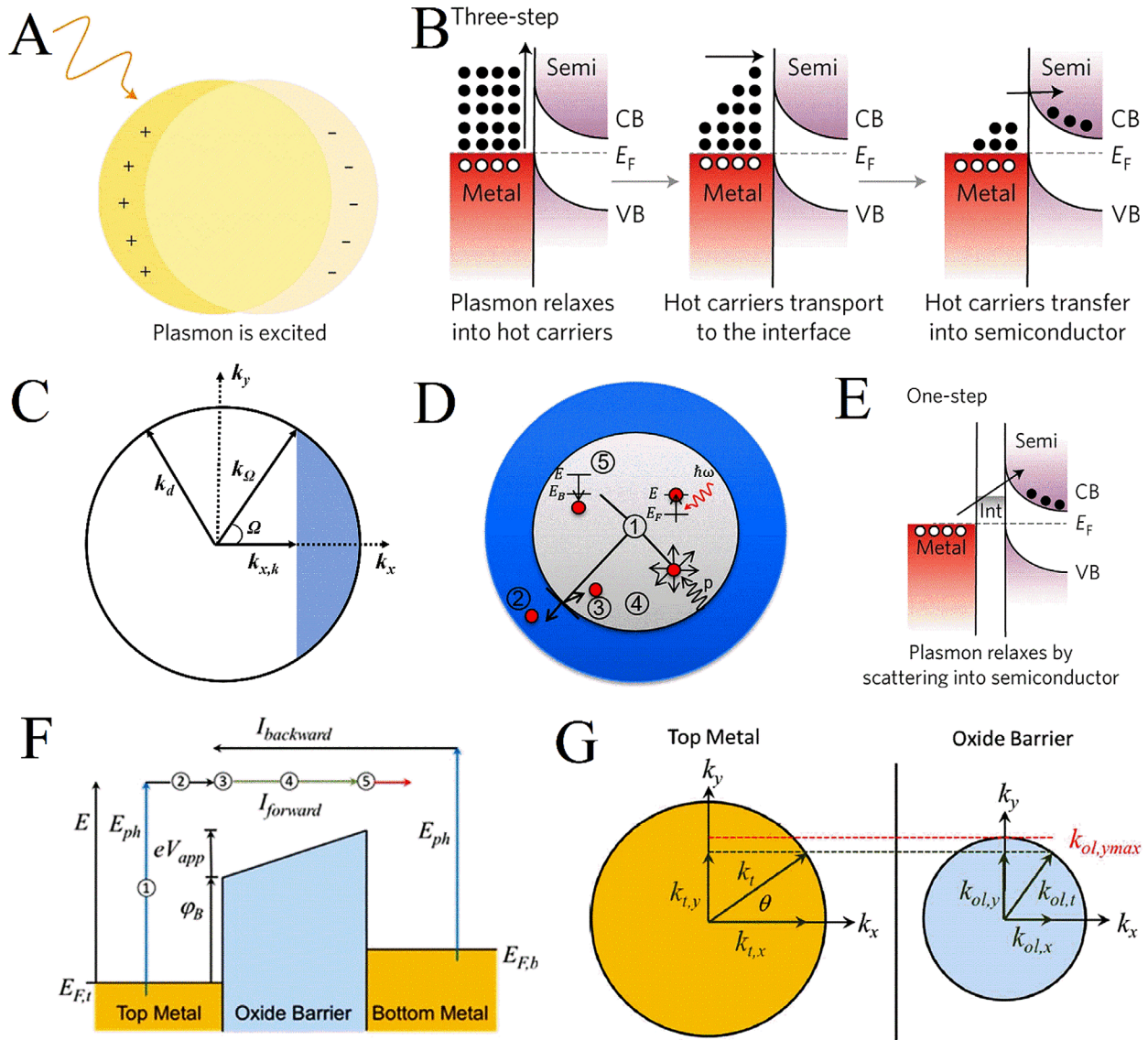


**Figure 4.** A) Schematic of the excitation of surface plasmons. B) Three-step phenomenal model: hot carrier generation upon the decay of surface plasmon, transport to Schottky interface and inject into the conduction band of a semiconductor. Reproduced with permission.<sup>[48]</sup> Copyright 2017, Springer Nature. C) Cross-section of the hot carrier emission cone that terminates on the surface of the spherical cap. D) Schematic of the hot carrier transport in the metallic nanostructure considering the electron–electron, electron–photon scattering, and reflection at boundary. Reproduced with permission.<sup>[49]</sup> Copyright 2018, American Chemical Society. E) Schematic of one-step hot carrier extraction by directly scattering the oscillating electrons into a semiconductor. Reproduced with permission.<sup>[48]</sup> Copyright 2017, Springer Nature. F) Schematic of the five-step hot carrier extraction process in a metal–insulator–metal diode. G) Schematic of the momentum conservation at each stage for injection into the oxide layer. Reproduced with permission.<sup>[22]</sup> Copyright 2014, American Chemical Society.

### 3. Hot Carrier Photodetectors from Ultraviolet to Infrared Bands

Hot carrier photodetectors convert hot carriers from metals into a photocurrent by forming a Schottky barrier with a semiconductor or tunneling through an MIM junction,<sup>[22]</sup> which are distinguished from the conventional semiconductor photodetectors. By modulating the interfacial barrier, the responsive spectral range of hot carrier photodetectors can cover from middle ultraviolet to middle-infrared (MIR) bands. In addition to using the metallic nanostructures to enhance the responsivity, the hot car-

rier photodetectors in planar configurations have been developed to simplify the fabrication and reduce the cost for the practical application.

#### 3.1. Plasmonic Hot Carrier Photodetection in Ultraviolet and Visible Bands

Ultraviolet photodetection plays an important in very broad application fields such as flame detection, UV astronomy, homeland security, and biological sensing.<sup>[21,51]</sup> Traditional UV pho-

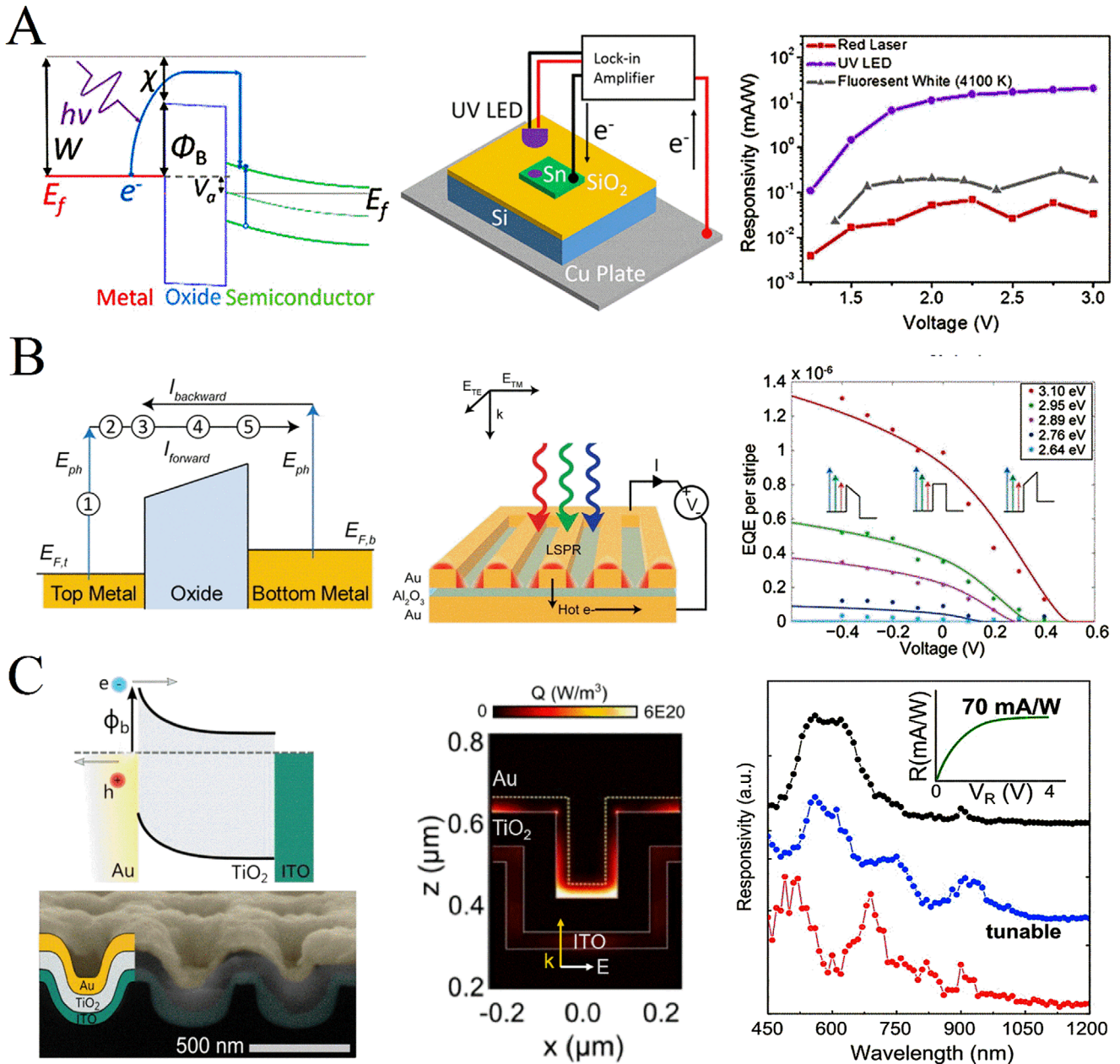


**Figure 5.** Plasmonic hot carrier photodetection in ultraviolet and visible bands. A) Energy band diagram, schematic, and responsivity spectra of Sn/SiO<sub>2</sub>/Si system. Reproduced with permission.<sup>[21]</sup> Copyright 2018, American Chemical Society. B) Energy band diagram, schematic, and EQE of the MIM device. Reproduced with permission.<sup>[22]</sup> Copyright 2014, American Chemical Society. C) Band diagram, SEM, hot electron generation, and responsivity spectra of the plasmonic-crystal-based photodetector. Reproduced with permission.<sup>[24]</sup> Copyright 2015, American Chemical Society.

photodetectors are based on wide-bandgap semiconductor materials such as [Al, indium (In)] Gallium nitride (GaN), diamond, and silicon carbide (SiC), which have larger bandgaps over 3.8 eV.<sup>[21]</sup> However, the surface and crystalline quality, n- and p-type doping along with the high-temperature processing limit the applications of traditional UV photodetectors. Another way is to incorporate solar-blind band-pass UV filters with Si photodetectors, which perform poorly due to the limited optical bandwidth and the inevitable vibration and percussion.

To overcome these challenges, the hot carrier photodetectors based on metal (Sn)–insulator (SiO<sub>2</sub>)–semiconductor (Si, MIS) system is proposed, which has an interfacial barrier of  $\approx 3.8$  eV.<sup>[21]</sup> Figure 5A shows that hot electrons are generated in Sn with an energy distribution from Fermi level ( $E_f$ ) to incident photon energy above  $E_f$ . Only the hot electrons with an energy greater than the potential barrier can transfer across the interface, inject into Si and generate photocurrent, achieving the solar-blind UV photodetection. For an efficient hot electron generation, transport,



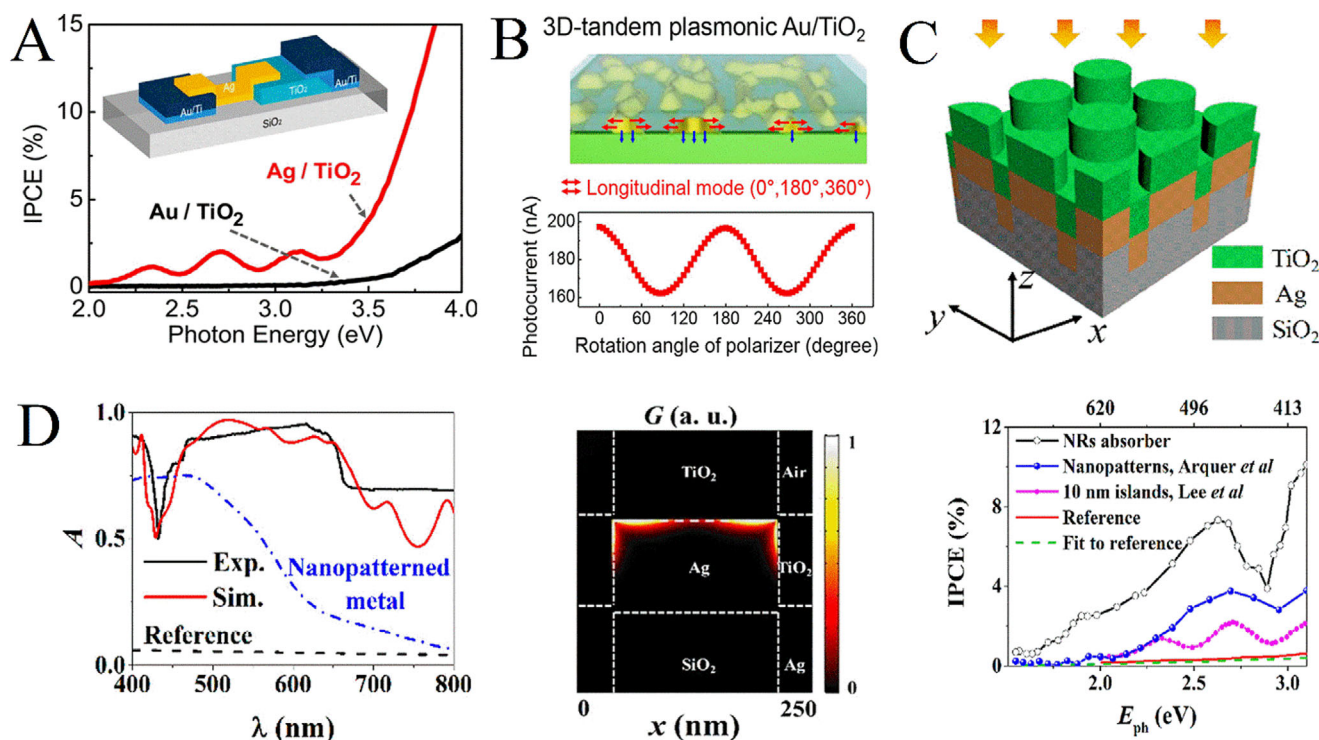


**Figure 6.** A) Schematic diagram and IPCE of the Au–TiO<sub>2</sub> nanodiode. Reproduced with permission.<sup>[52]</sup> Copyright 2014, American Chemical Society. B) The hot electron transport path and the effect of polarization angle on the photocurrent in the tandem-structured plasmonic nanodiode. Reproduced with permission.<sup>[53]</sup> Copyright 2018, American Chemical Society. C) Schematic diagram of hot carrier generation distribution in the 3D tandem structure and D) the optical response, the hot electron generation distribution, and IPCE spectra comparison. Reproduced with permission.<sup>[54]</sup> Copyright 2018, American Chemical Society.

and emission process, the metallic absorber with the high-density state near  $E_f$ , the photon management of pseudoperiodic nanodot arrays, and interfacial defect passivation are employed. At  $\lambda = 269$  nm, the measured responsivity is up to  $29 \text{ mA W}^{-1}$ , which is three orders of magnitude higher than that in the visible band. With a relatively lower barrier of 2.6 eV in the Au/Al<sub>2</sub>O<sub>3</sub>/Au junction, the visible and UV photodetection is realized as shown in Figure 5B.<sup>[22]</sup> One of the metallic contacts is reshaped into stripes to support surface plasmons and improve the hot electron generation efficiency, realizing the ultracompact, wavelength, and polarization-dependent hot-electron photodetector. The detection limit can be extended to the visible regime by replacing the intermediate insulator layer (e.g., SiO<sub>2</sub>/Al<sub>2</sub>O<sub>3</sub>) with semiconductor materials (e.g., TiO<sub>2</sub>), which results in a lower barrier height  $\approx 0.7$  to 1.1 eV.<sup>[10,24,49]</sup> With the platform of quasi-3D plasmonic crystal, the tunable and multiband photoresponse across the visible and near-infrared band is reported, as illustrated in Figure 5C. The localized surface plasmon modes, the lattice modes, and the hybrid modes together give rise to intense plasmonic resonances with hot electrons generated near the Schottky interface. The responsivity is up to  $70 \text{ mA W}^{-1}$  under the incidence of  $\lambda = 640$  nm at the reverse bias of 4 V.

With a corrugated Ag surface on TiO<sub>2</sub>, Figure 6A shows that the photocurrent is enhanced by exciting surface plasmons, which decay into energetic hot electrons.<sup>[52]</sup> The thickness and morphology of the Ag layer are the key factors for photocurrent enhancement. Furthermore, the effect of light polarization on

the photocurrent is investigated in the systems of 2D plasmonic Au/TiO<sub>2</sub> and 3D tandem structures by further coating a layer of TiO<sub>2</sub>.<sup>[53]</sup> It is found from Figure 6B that the photocurrent is improved in the 3D tandem structure since the hot electrons diffusing toward all directions can be extracted. In addition, for the plasmonic structure, the maximum photocurrent is obtained in transverse mode with an electric field aligned with the short side of the plasmonic structures, orthogonal to the Schottky interface. For the tandem structure, the photocurrent is much higher in longitudinal mode since the electric field is stronger and more hot electrons are generated. Since the plasmonic structures usually support only narrowband plasmon resonances, the metallic nanorod arrays (Figure 6C) are proposed, which show a broadband super absorption (Figure 6D), i.e., an average absorption of 0.8 across the visible band.<sup>[54]</sup> The hot electrons are preferentially generated near the Schottky interface and the 3D Schottky junction increases the allowed hot-electron momentum space at the vertical interface. The incident photon-to-electron conversion efficiency (IPCE) is predicted to be over 30 times enhanced relative to the planar reference.

### 3.2. Plasmonic Hot Carrier Photodetection in Infrared Band

Due to the limitation of the energy bandgap, the traditional Si photodetector does not work in the telecommunication bands  $\approx 1.31$  and  $1.55 \mu\text{m}$ . Thus, extending the working band of Si-

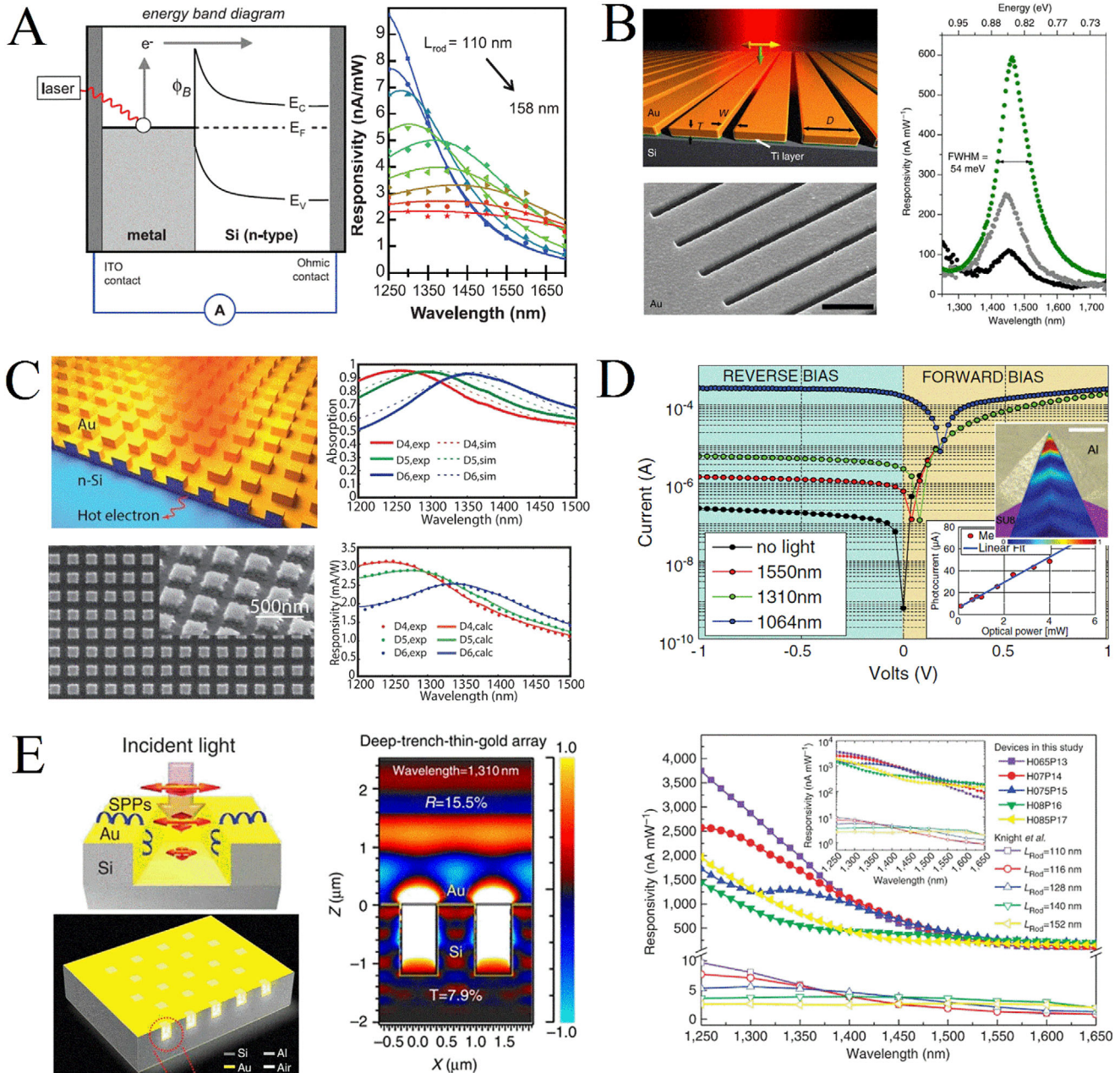


**Figure 7.** Plasmonic hot carrier photodetection in near-infrared. A) The energy band diagram and responsivity spectra of the hot electron device based on Au nanoantenna and silicon. Reproduced with permission.<sup>[13]</sup> Copyright 2011, American Association for the Advancement of Science. B) Schematic, SEM, and responsivity spectra of the narrowband hot-electron photodetector based on metallic gratings. Reproduced with permission.<sup>[6]</sup> Copyright 2013, Springer Nature. C) Schematic diagram, absorption, and responsivity spectra of the hot-electron photodetector based on the metamaterial perfect absorber. Reproduced with permission.<sup>[56]</sup> Copyright 2014, American Chemical Society. D) The current–voltage curve of the hot-electron photodetector is based on the silicon pyramid structure with the electric field intensity distribution and the effect of power on photocurrent shown in the inset. Reproduced with permission.<sup>[57]</sup> Copyright 2015, OSA Publishing. E) Schematic diagram, electric field intensity, and responsivity spectra of the broadband hot-electron photodetector based on a deep trench thin metal structure. Reproduced with permission.<sup>[58]</sup> Copyright 2014, Springer Nature.

based photoconversion device into the long-wave near-infrared (LW-NIR) and MIR bands is of significant importance in the military, remote sensing, communication, and other related fields.<sup>[8,28,55]</sup> In 2011, the metallic nanoantennas on the n-Si substrate were demonstrated to simultaneously function as a light absorber and photodiode.<sup>[13]</sup> Hot electrons are generated in the

optical antenna arising from the decay of surface plasmons, subsequently, transfer across the Schottky junction into the conduction band of Si (see **Figure 7A**). The detection wavelength is extended to  $\approx 1650$  nm in the Si-based photodetector, with absorption and responsivity spectra tuned by controlling the nanoantenna geometry. In principle, the low barrier height of 0.5 eV is

expected to permit the detection of the entire short-wave near-infrared (SW-NIR). On this basis, the metallic gratings are employed to excite surface plasmons propagating on the upper and lower surfaces of the gratings, yielding a strong, narrowband and resonant absorption, with most of the hot electrons generated at the bottom surface of the gold layer, as shown in Figure 7B.<sup>[6]</sup> As a result, the responsivity is improved to  $0.6 \text{ mA W}^{-1}$  and the internal quantum efficiency (IQE, 0.2%) is 20 times that in the previously reported antenna-based device.<sup>[13]</sup>

The concept of a metamaterial perfect absorber is demonstrated to achieve a near-unity optical absorption within a thin Au film of 15 nm, which simultaneously leads to efficient hot electron generation and injection processes.<sup>[56]</sup> The broadband, polarization-insensitive, and omnidirectional hot-electron photodetector with a responsivity of  $3 \text{ mA W}^{-1}$  is realized, as shown in Figure 7C. The silicon pyramids have also been demonstrated to concentrate light on a small area at the top surface, where the metal layer is deposited (Figure 7D).<sup>[57]</sup> The improved hot electron generation rate along with the relaxation of electron momentum mismatch results in responsivity of  $\approx 30 \text{ mA W}^{-1}$  at the wavelength of 1064 nm. In addition, the 3D antennas: deep-trench/thin-metal (DTTM) active antenna structures are developed to enhance the responsivity of hot-electron photodetector by exploiting the surface plasmons, 3D Schottky interface with a large area on both the surface and vertical sides of DTTM (Figure 7E).<sup>[58]</sup> It shows that the electric field intensity is large within the near field in the deep-trench arrays and the responsivity is two or three orders of magnitude larger than that of the previously reported nanoantenna-based devices.<sup>[13]</sup> The high, broadband and polarization-insensitive responsivity have a great potential in photodetection and image detection.

To further improve the responsivity of the grating-based device, the free-carrier absorption in highly doped p-type Si is combined with hot carrier photodetection (Figure 8A).<sup>[59]</sup> Free-carrier absorption is an intraband transition of the carrier within the valence or conduction band of the semiconductor, which is usually considered to be a parasitic loss since it does not contribute to a photocurrent. However, integrated with hot carrier photodetector, the unbiased responsivity is improved by 3–5 times and larger than  $1 \text{ A W}^{-1}$  at a relatively low bias of 93 mV. For high-performance hot-electron photodetectors, both optical absorption and electron emission are crucial factors to be addressed. The plasmonic absorber consisting of a monolayer of Au nanoparticles,  $\text{TiO}_2$ , and thick Au electrode exhibits a broadband near-infrared absorption and efficient hot electron transfer via an all-around Schottky emission path.<sup>[60]</sup> Figure 8B indicates that the responsivity is up to  $3.3 \text{ mA W}^{-1}$  at the wavelength of 1500 nm under a reverse bias of 5 V. Alternatively, the plasmonic nanostructure consisting of a thin Au film on random Si nanoholes shows a high and broadband absorption, accompanied by a strong electric field localization. Both photoelectric hot-electron ejection and photothermal hot electron relaxation contribute to the broadband photon-energy conversions.<sup>[61]</sup> The photoresponse contribution from the photoelectric hot electron ejection and photothermal hot electron relaxation can be distinguished by controlling the light radiation exposure time when conducting the current–voltage measurement. Figure 8C shows that under a reverse bias of 5 V, the photoresponse contribution from hot electron photothermal effect is closed to that from the

photoelectric hot electron injection. At a small forward bias, the photoresponse contribution from photoelectric hot electron injection is negligible and the photothermal hot electron relaxation effect contributes to the total responsivity. The unbiased responsivities are around  $1.5\text{--}13 \text{ mA W}^{-1}$  at wavelengths ranging from 1100 to 1500 nm. To conclude, the high optical absorption combined with an efficient hot electron transfer process are requisites for high-performance hot-electron photodetectors. Further enhancement in the responsivity with a simplified fabrication has to be realized to compete with the commercially available III–V/II–VI compound near-infrared photodetectors.

### 3.3. Hot Carrier Photodetectors in Planar Configurations

All the above-mentioned plasmonic hot-carrier photodetectors employ metallic nanostructures to improve the hot electron generation and transport efficiency by the excitation of surface plasmons. However, the metallic nanostructures are usually complex with a high fabrication challenge, which hinders the practical application of hot carrier photodetectors. Therefore, part of the attention goes back to the planar scenarios for cost-effective strategies.

To simplify the device geometry, a new scheme to extract hot electrons is proposed in Figure 9A by using transparent conductive oxide (TCO) in a planar ITO–insulator–metal configuration.<sup>[62]</sup> Since ITO is transparent in visible light with minimal absorption,  $\approx 80\%$  of light is absorbed in the metal layer adjacent to the metal/insulator interface independent of incident angle, leading to highly asymmetric light absorption and hot carrier generation. The measured wavelength-dependent open-circuit voltage is one order of magnitude larger than that of the previous metal–insulator–metal designs with a predicted power conversion efficiency  $> 10\%$  under optimum conditions. However, the planar system shows a weak light-trapping capability, e.g.,  $A \sim 10\%$  for  $\lambda > 600 \text{ nm}$ . To further improve the optical absorption and photoconversion efficiency, the core electrical section of the TCO–semiconductor–metal structure is sandwiched between two asymmetrically distributed Bragg reflectors (DBRs) and a lossless buffer layer.<sup>[63]</sup> Figure 9B shows that the resonant wavelength and strength can be easily tuned by the buffer layer thickness and the number of top DBR pairs. The asymmetric microcavity leads to enhanced absorption of 92% in the metallic film of 20 nm. The highly asymmetric generation of hot electrons results in a strongly unidirectional photocurrent and a responsivity that is more than an order of magnitude larger than that of the planar reference without a microcavity. The responsivity could be 2.5 times larger than that based on the conventional gratings and multiband photodetection can be realized by exciting high-order defect modes with a thick buffer layer. Since two DBRs are required to form the microcavity, the microcavity-based hot-electron system is relatively thick and brings a challenge for fabrication. Thus, a type of surface plasmons named Tamm plasmons formed at the boundary between a metal and DBR are introduced into the design of the hot-electron photodetector (TP-HE PD).<sup>[64]</sup> In contrast to conventional SPs, TPs can be optically excited from free space under any polarizations without the vector-matching treatments by gratings, nanoparticles, or prisms. The planar hot-electron photodetector based on TPs consists of a DBR

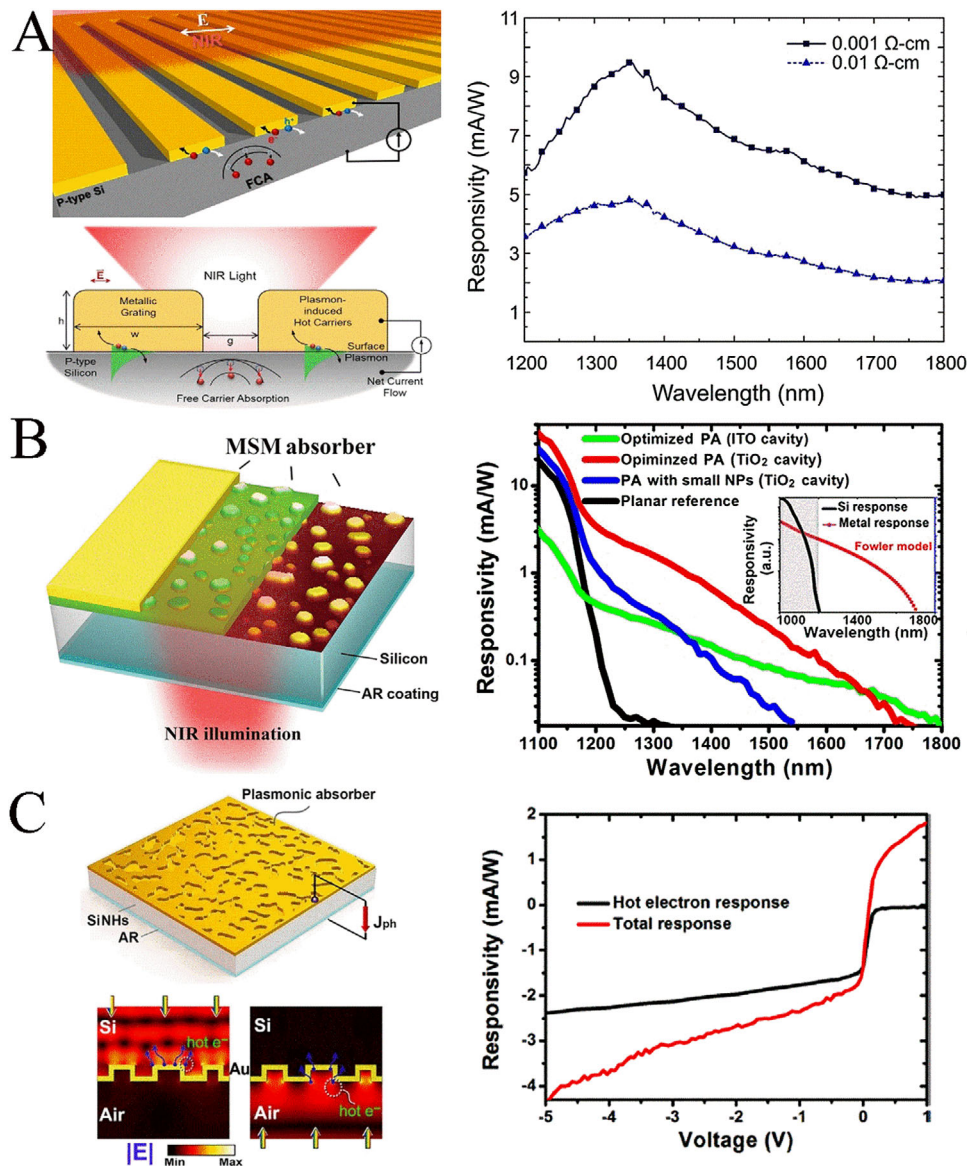


**Figure 8.** A) Schematic, the principle diagram of free carrier absorption and responsivity spectrum in the plasmonic hot-electron photodetector. Reproduced with permission.<sup>[59]</sup> Copyright 2018, American Chemical Society. B) The schematic diagram and responsivity spectrum of the hot-electron photodetector based on plasmonic absorbers. Reproduced with permission.<sup>[60]</sup> Copyright 2017, Wiley-VCH. C) Schematic diagram, the electric field distribution, and responsivity of the hot-electron photodetector as a function of voltage under light radiation exposure time of 1 s and 2 min. Reproduced with permission.<sup>[61]</sup> Copyright 2018, American Chemical Society.

and hot electron collection layers in metal/semiconductor/metal configuration, as shown in Figure 9C. More than 87% of light is absorbed by the top metal layer of 25 nm, which enables a strong and unidirectional photocurrent with a responsivity higher than that based on the conventional nanostructured system. Moreover, the simplified planar TP system shows a high resonance tunability, robustness in oblique incidence, and the possibility for extended functionalities. Recently, the concept of TP-HE PD is experimentally demonstrated in the gold/titanium-zinc oxide-indium tin oxide (Au/Ti-ZnO-ITO) section, based on the modified Ge/SiO<sub>2</sub> DBR structure (Figure 9D).<sup>[65]</sup> The peak responsivity is 8.26 nA/mW at  $\lambda = 1581$  nm and decreases by more than 80% when the illumination wavelength is var-

ied by 52 nm, realizing a high modulation wavelength-selective photodetector.

Besides the conventional plasmonic element metals such as Au, Ag, Al, the highly conductive material of titanium nitride (TiN) has been explored in hot carrier photodetection by the direct excitation of hot carriers without exciting SPs. The planar device in Figure 10A consists of TiN-ZnO-TiN trilayers, a unidirectional photocurrent across the visible light is observed due to the asymmetric absorption between the top and bottom TiN layers.<sup>[66]</sup> Compared to the same configuration of using Au, the photocurrent is one order of magnitude larger due to the higher light absorption in TiN and the formation of Ohmic contact at the TiN-ZnO interface. By exploiting a zeroth-order Fabry-Perot

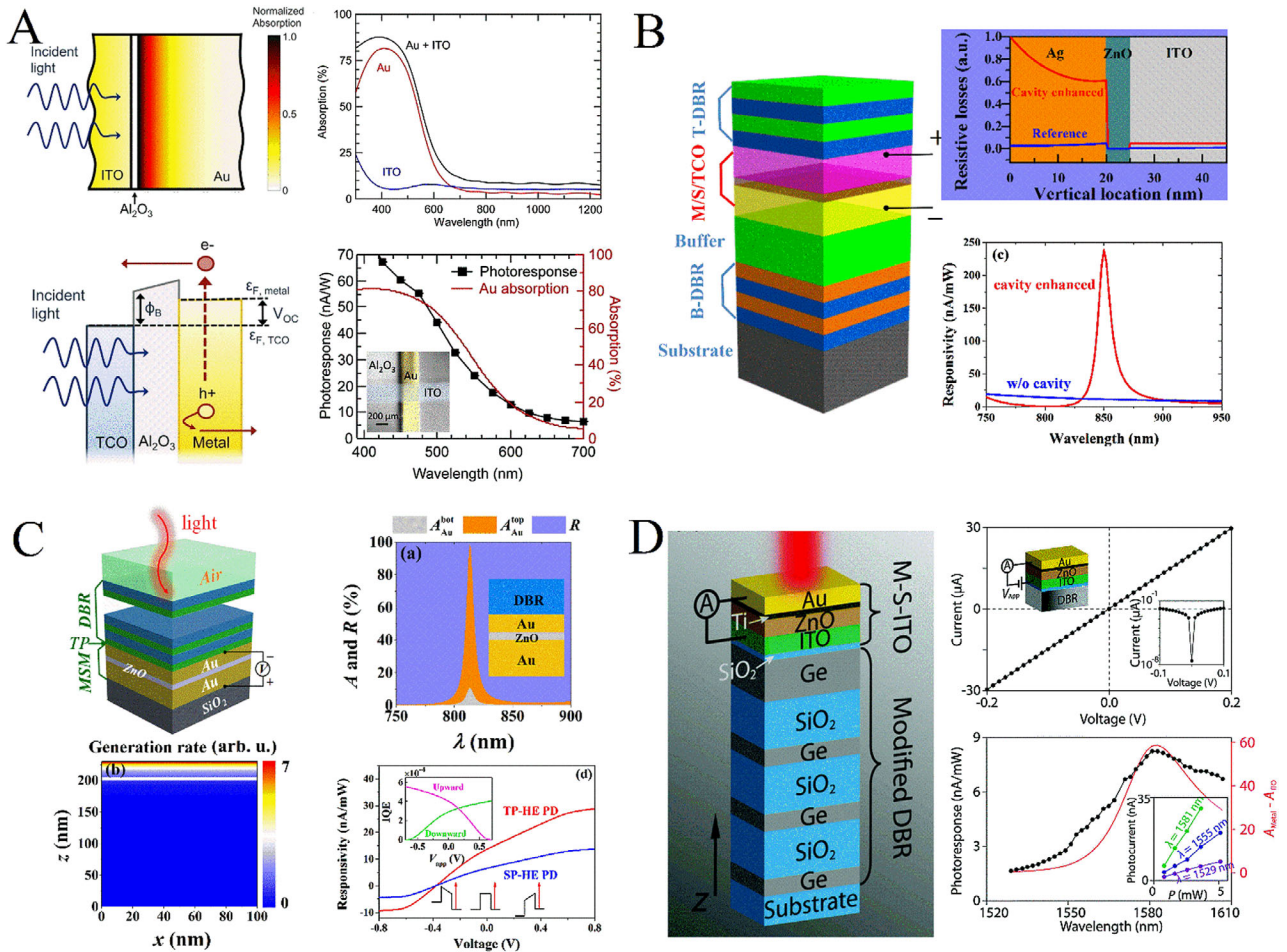


**Figure 9.** Planar hot carrier photodetection. A) Schematic, energy diagram, optical response, and responsivity of the hot-electron photodetector based on transparent conductive oxide. Reproduced with permission.<sup>[62]</sup> Copyright 2015, American Chemical Society. B) The microcavity integrated hot-electron photodetector with the hot electron generation distribution and responsivity spectrum. Reproduced with permission.<sup>[63]</sup> Copyright 2016, Royal Society of Chemistry. C) Schematic, optical response, hot electron generation distribution, and responsivity of the hot-electron photodetector based on Tamm plasmons. Reproduced with permission.<sup>[64]</sup> Copyright 2017, American Chemical Society. D) Schematic and measured electrical response of the hot-electron photodetector based on Tamm plasmons. Reproduced with permission.<sup>[65]</sup> Copyright 2019, Royal Society of Chemistry.

resonance in ultrathin metal films, Figure 10B shows that nearly 80% absorption of broadband NIR light is obtained, which results in responsivity of  $10^{-6}$ – $10^{-4}$  A W<sup>-1</sup> at zero applied bias for wavelengths of 1.2–1.5  $\mu\text{m}$ , respectively.<sup>[55]</sup> The application of hot carrier photodetector in imaging detectors is demonstrated with superior performance compared to commercial Si detectors under room-temperature operation below the semiconductor bandgap. Furthermore, the planar dual-layer system comprised of a transparent dielectric film on an absorptive substrate is demonstrated to have a broadband, strong, polarization/angle-insensitive absorption across the longwave near-infrared band. The application in hot-carrier photodetection is explored, which shows the responsivity and detectivity can even be an order of magnitude higher than those based on metallic nanostructures.<sup>[67]</sup> Moreover, the planar hot carrier photodetector based on amorphous Ge and TiN thin film is demonstrated in Figure 10C.<sup>[68]</sup> Attributed to the broadband absorption of TiN and the hot carrier transfer across TiN/Ge junction, the photodetection limit can be up to 2600 nm with a specific detectivity of  $6.32 \times 10^5$  Jones at  $\lambda = 2000$  nm.

## 4. Thermodynamic Losses and Strategies for High-Performance Hot Carrier Photodetectors

Despite the enormous efforts, the photoconversion efficiencies of hot carrier devices are still low. In fact, a number of optical, electrical, and material factors together lead to the substantial losses of hot electrons during the generation, transport, and emission processes.<sup>[69]</sup> Thus, the thermodynamic loss mechanisms of hot electrons in the photoemission process play a key role in exploring the possible solutions to realize high-efficiency hot-electron photodetectors.

### 4.1. Hot Carrier Loss Analysis and Potential Solutions

Based on the modified three-step phenomenological model by further introducing additional physics to address the resistive dissipation, the thermalization loss, and the electron reflections at the Schottky interface, the thermodynamic analysis shows that

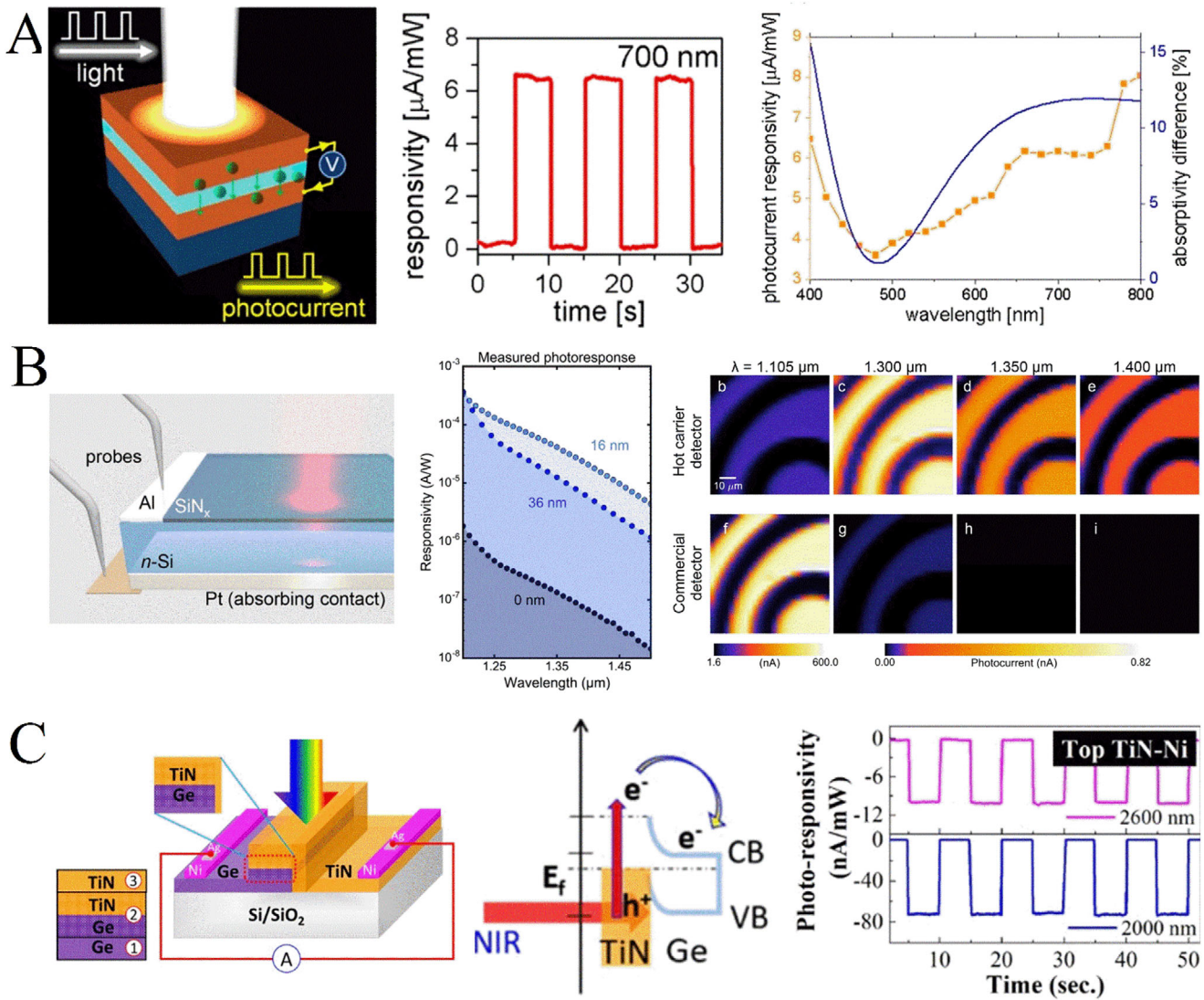


**Figure 10.** A) Schematic and responsivity of the hot-electron photodetector based on TiN/ZnO/TiN. Reproduced with permission.<sup>[66]</sup> Copyright 2016, American Chemical Society. B) Schematic and responsivity of the hot-electron photodetector based on nanometer-scale optical coatings. Reproduced with permission.<sup>[55]</sup> Copyright 2018, American Chemical Society. C) Energy diagram, schematic, and responsivity of the hot-electron photodetector based on the TiN/Ge heterostructure. Reproduced with permission.<sup>[68]</sup> Copyright 2019, American Chemical Society.

a number of optical, electrical, and material factors lead to the substantial losses of hot electron energies.<sup>[69]</sup> It is found that the low optical absorption, resistive dissipation, nearly uniform hot-electron energy distribution, rapid hot-electron thermalization, and momentum conservation in interfacial electron transfer are the key reasons leading to the extremely low hot-electron photo-conversion efficiency. The detailed mechanisms of hot electron energy losses are categorized into three kinds occurring in the hot electron generation, transport, and emission processes. The inherent physical limiting factors, as well as the potential solutions, are presented in **Figure 11A**. Accordingly, the corresponding solution for each limiting factor can be explored to improve hot carrier device performance. For the hot electron generation engineering, the hot electron generation rate can be significantly improved by exciting TPs in the planar system of DBR/Au as shown in **Figure 11B**. At TP resonance, light propagates

with the interface of DBR/Au with the electric field highly confined in the region and exponentially decayed away from the interface. The near-perfect light absorption results in a high hot electron generation rate accompanied by a favorable hot-electron spatial distribution, i.e., most hot electrons are generated close to the Schottky interface. In addition, the nanostructured hyperbolic metamaterials in **Figure 11C** are proposed to realize broadband and angle-independent light absorption at infrared and visible bands.<sup>[70]</sup> The vertically integrated hot-electron devices with ultrathin metal films less than the electromagnetic skin depth exhibit an external quantum efficiency approaching the physical limit.

The first-principles calculations show that part of the losses in the metal can proceed through classic resistive dissipation with energies converted into heat, instead of hot carriers.<sup>[42]</sup> **Figure 11D** shows that for the bulk Au, the resistive dissipation com-

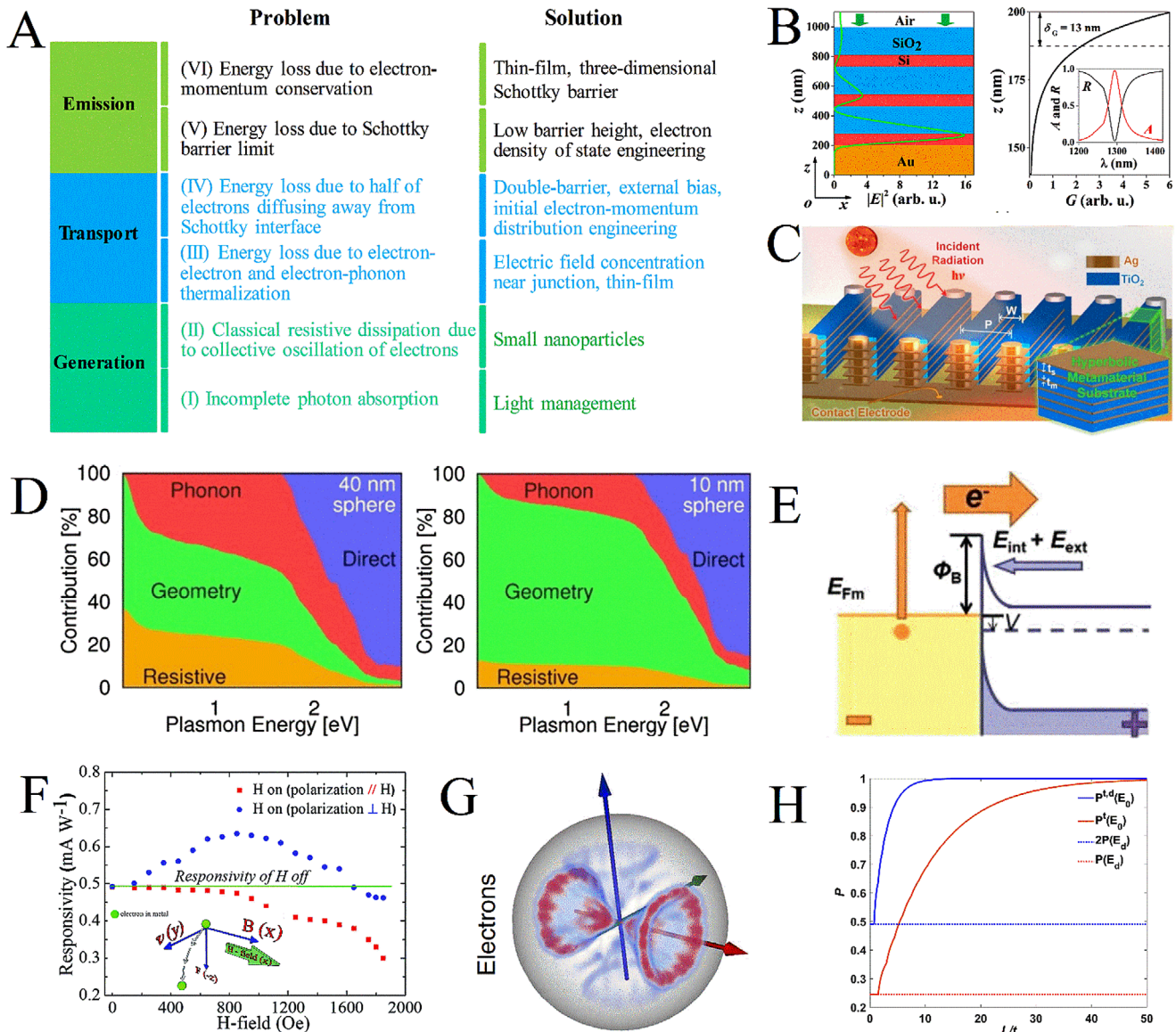


**Figure 11.** A) Thermodynamic losses and solutions in hot-electron conversion. B) Schematic diagram of the proposed Tamm plasmon-induced hot electron system with the optical response and hot electron generation distribution. Reproduced with permission.<sup>[69]</sup> Copyright 2019, Elsevier Ltd. C) Schematic diagram of the broadband hot-electron photodetector based on the metal–semiconductor hyperbolic metamaterials. Reproduced with permission.<sup>[70]</sup> Copyright 2016, Elsevier Ltd. D) Relative contributions of the resistive losses, direct, geometry-assisted, and phonon-assisted transitions in 40 and 10 nm spheres. Reproduced with permission.<sup>[42]</sup> Copyright 2016, American Chemical Society. E) Schematic diagram of Schottky interface band structure under negative external bias. Reproduced with permission.<sup>[71]</sup> Copyright 2017, American Institute of Physics. F) The schematic diagram of magnetic field effect and the responsivity as a function of magnetic field strength. Reproduced with permission.<sup>[72]</sup> Copyright 2016, Royal Society of Chemistry. G) Plasmonic hot carrier energy and momentum-direction distribution in Al. Reproduced with permission.<sup>[41]</sup> Copyright 2014, Springer Nature. H) Transport efficiency of the thick-film single-barrier, thick-film double-barrier, thin-film single-barrier, and thin-film double-barrier hot-electron photodetectors.

petes with phonon-assisted transitions and accounts for  $\approx 30\text{--}50\%$  below the interband threshold. The resistive dissipation can be reduced to  $\approx 10\%$  by decreasing particle size to  $\approx 10$  nm diameter spheres. Direct transition dominates above the interband threshold even for small spheres. In addition, applying an external electric or magnetic field can modulate the optoelectronic response of hot carrier devices. For example, Figure 11E shows that the injection of hot electrons can be facilitated by the external

electric field under negative external bias, resulting in a significant photocurrent enhancement by orders of magnitude in the nanosized gold/strontium titanate system.<sup>[71]</sup> When a magnetic field is applied to the hot carrier photodetector based on nickel (Ni)/Si Schottky diode in the DTTM active antenna structure, Figure 11F shows that the Lorentz force and anisotropic magnetoresistance (AMR) can assist the hot-electron transfer into Si layer.<sup>[72]</sup> It is found that by applying a low magnetic field strength

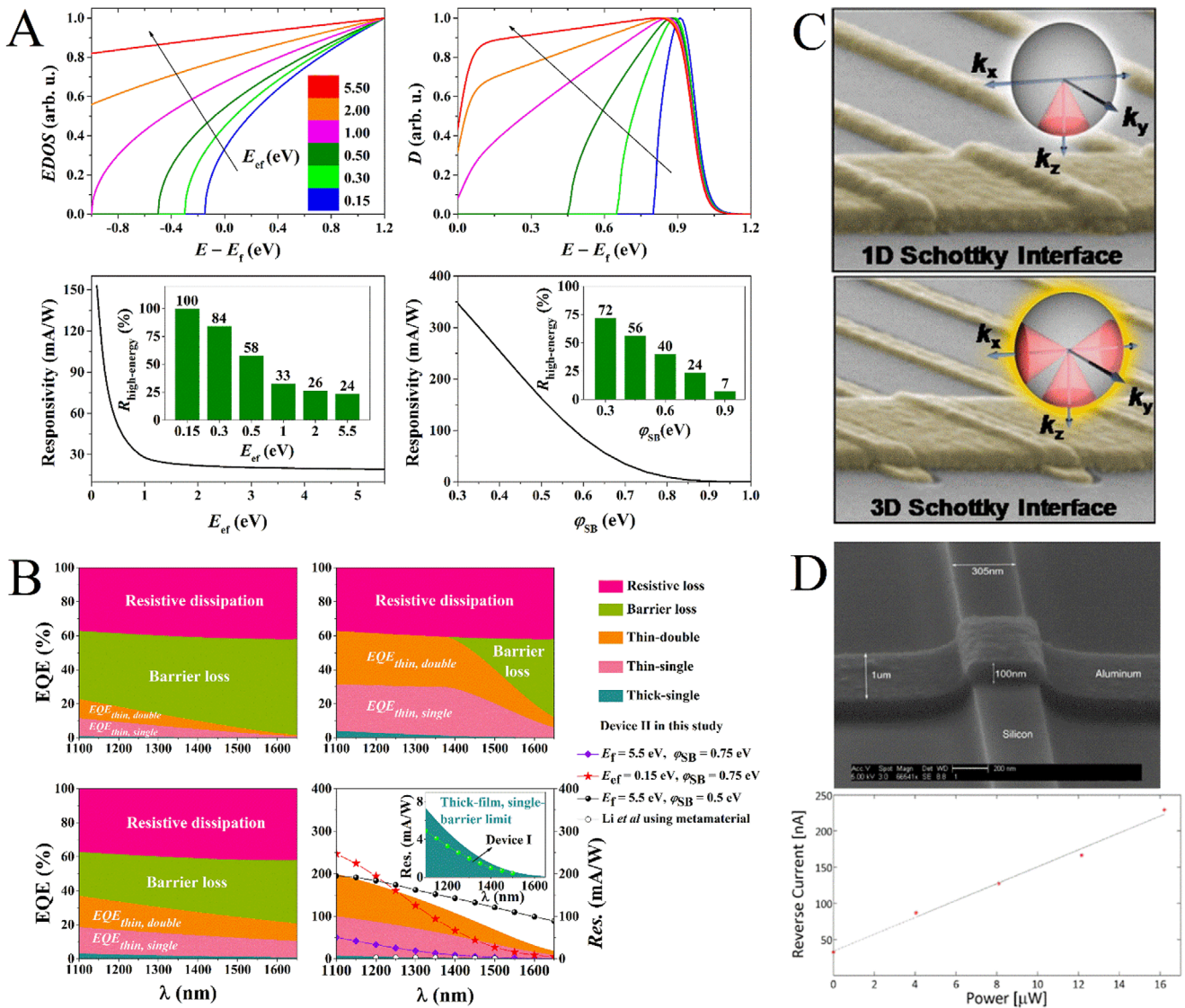


**Figure 12.** A) Engineering of the electronic density of state (EDOS) and Schottky barrier for efficient hot electron collection. B) EQE limits and responsivity spectra of the planar hot electron device with different effective Fermi levels and Schottky barrier heights. Reproduced with permission.<sup>[69]</sup> Copyright 2019, Elsevier Ltd. C) Improving the hot-electron transfer efficiency by embedding plasmonic NWs into Si substrate. Reproduced with permission.<sup>[76]</sup> Copyright 2013, American Chemical Society. D) The measured responsivity is  $\approx 2$  orders of magnitude higher by introducing the surface roughness at the boundary of the Schottky junction. Reproduced with permission.<sup>[77]</sup> Copyright 2012, OSA Publishing.

of less than 800 Oe, the responsivity is improved due to the AMR effect and the Lorentz force in the Ni film. It is acknowledged that the initial momentum distribution is particularly important in hot carrier injection efficiency. For direct transitions in noble metals, the initial momentum distributions are strongly anisotropic and dominated by the crystal direction;<sup>[41]</sup> while in Al, the carrier momentum distribution is controlled by the polarization direction, as shown in Figure 11G. For hot carrier transport, with a double-barrier configuration in Figure 11H, all hot electrons will diffuse toward the Schottky interfaces.<sup>[20]</sup> At the same time, with a thin metal film, the hot electron emission efficiency is expected to be boosted due to the multiple electron reflections between the internal metal surfaces.

Considering the initial hot carrier energy distribution plays a key role in the injection process, **Figure 12A** shows that we can generate more high-energy hot electrons by engineering the effective Fermi level (the effective conduction band edge below the Fermi level of the metal).<sup>[69]</sup> By decreasing the effective Fermi level, the excited electrons are distributed in a higher and narrower energy range, leading to an enhanced responsivity.<sup>[73,74]</sup> In addition, the responsivity can also be improved with a low-energy Schottky barrier, which allows more hot electrons to accomplish the interfacial electron transfer process.<sup>[75]</sup> However, the dark current could be increased in this case and the trade-off between the responsivity and detectivity must be considered. The limiting external quantum efficiency (EQE) spectra of the



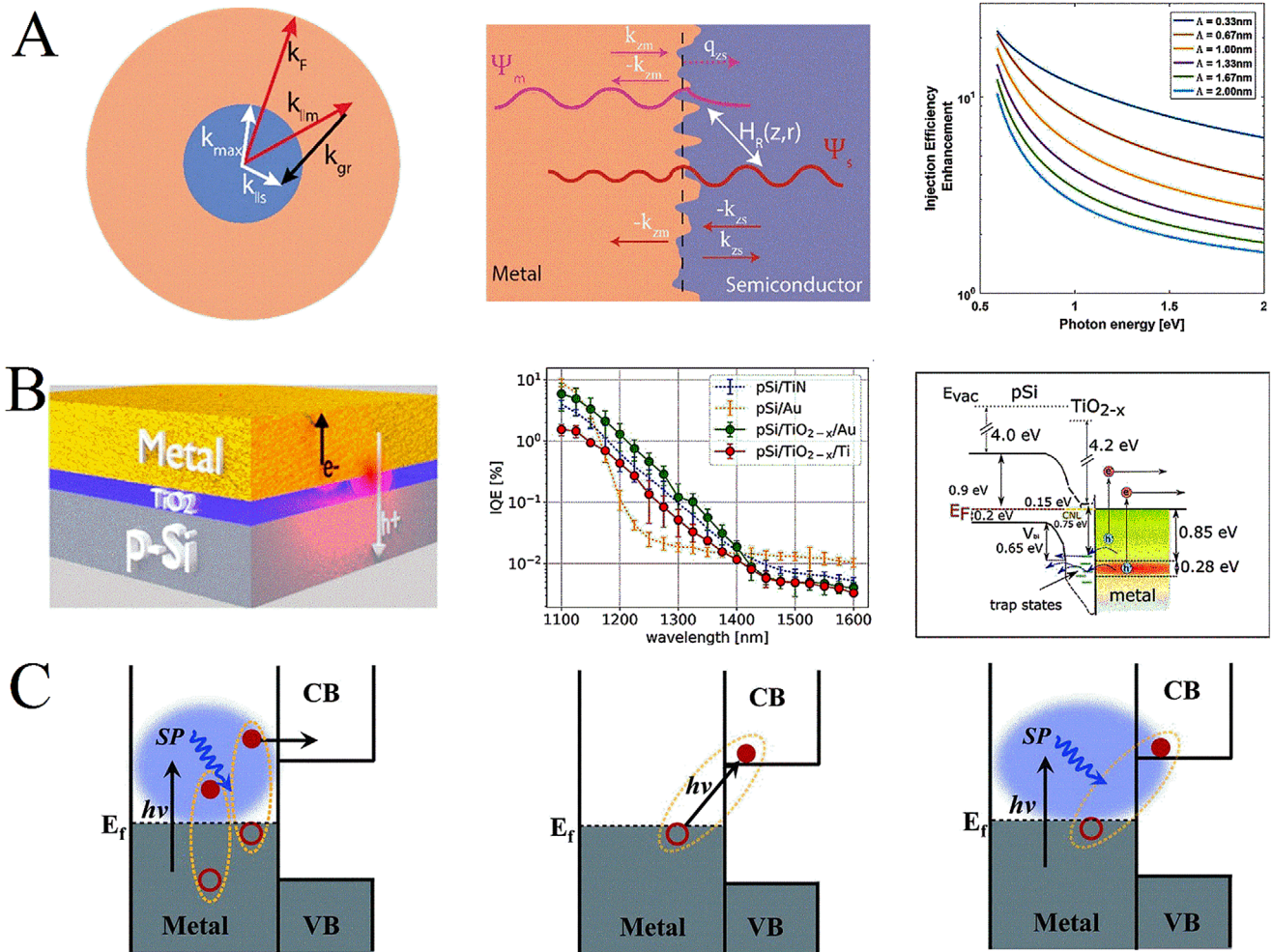


**Figure 13.** A) Theoretical study of surface roughness using a perturbative model. The injection efficiency can be enhanced by an order of magnitude by surface roughness on the scale of a few atomic layers. Reproduced with permission.<sup>[78]</sup> Copyright 2018, American Chemical Society. B) Schematic diagram, IQE spectra, and energy band diagram of the  $\text{TiO}_{2-x}$ -enhanced hot carrier photodetector. Reproduced with permission.<sup>[79]</sup> Copyright 2019, American Chemical Society. C) Metal-to-semiconductor charge-separation pathways: conventional plasmon-induced hot electron transfer mechanism, direct metal-to-semiconductor interfacial charge-transfer transition, and plasmon-induced metal-to-semiconductor interfacial charge-transfer transition. Reproduced with permission.<sup>[50]</sup> Copyright 2015, American Association for the Advancement of Science.

planar hot-electron devices under thick-film single-barrier, thin-film single-barrier, and thin-film double-barrier configurations are shown in Figure 12B, where the barrier and resistive losses are noted. It is clear that for the planar thick-film/single-barrier hot electron device, the limit of EQE is extremely low and can be improved with a thin-film metal.<sup>[20]</sup> With a low effective Fermi level or a low barrier height, the barrier loss can be eliminated or relieved. The responsivity of the hot electron device based on TPs is close to the theoretical limit of the thick-film single-barrier device. It is noted that the photoconversion efficiencies of the reported hot carrier devices are normally below 1%. By combing the optimized optoelectronic design, the modulated effective Fermi level, and Schottky barrier, the external quantum efficiency of hot carrier photodetectors can be up to 60% after the optical and electrical optimization. Another approach to improve the injection efficiency is to form a 3D Schottky barrier by embedding the plasmonic nanostructure within the semiconductor as shown in Figure 12C, which increases the momentum space for hot electron

emission.<sup>[76]</sup> Besides, it is experimentally demonstrated in Figure 12D that the responsivity of the waveguide-based hot-electron photodetector can be enhanced by  $\approx 2$  orders of magnitude by introducing the surface roughness of the Schottky junction.<sup>[77]</sup>

To further understand the physics behind the experimental observation, the role of surface roughness in enhancing the injection efficiency is investigated by a perturbative model.<sup>[78]</sup> It is shown in Figure 13A that the enhancement strongly depends on both mean height and correlation length of the roughness. Compared to the smooth interface, the injection efficiency can be enhanced by an order of magnitude with a surface roughness on the scale of a few atomic layers. It is predicted that the injection efficiency can even be over 10% in a few angstroms RMS roughness and higher for larger roughness. Recently, it is experimentally demonstrated that an amorphous  $\text{TiO}_{2-x}$  film of a few nanometers thick can be exploited to facilitate hot hole injection into the pSi via  $\text{TiO}_{2-x}$  trap states.<sup>[79]</sup> It is found from Figure 13B that the unbiased responsivity can be increased by  $\approx 1$  order of magnitude

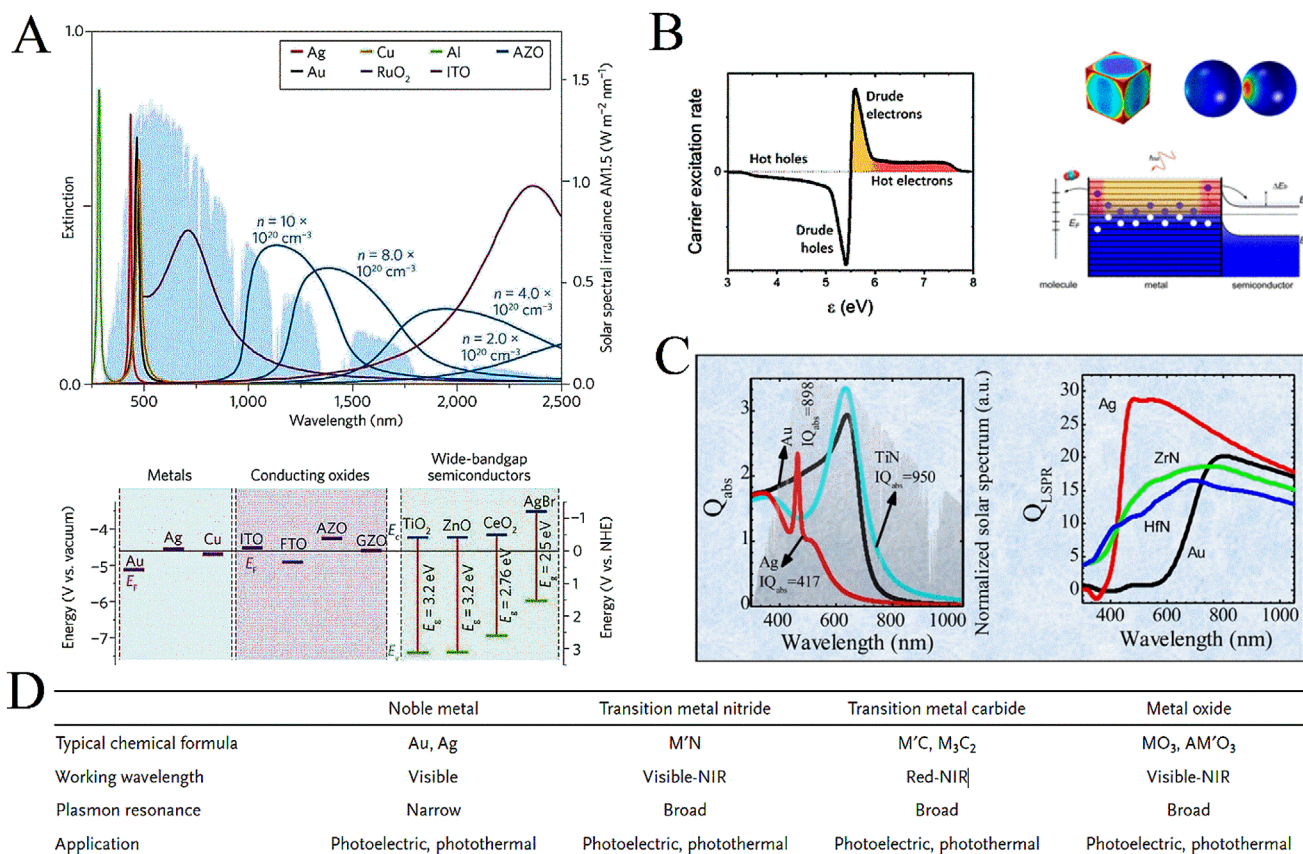


**Figure 14.** A) Optical extinction of metal and conducting oxides plasmonic nanostructures (top panel). Fermi level, conduction, and valence bands energy for selected metals, conducting oxides, and wide-bandgap semiconductors. Reproduced with permission.<sup>[8]</sup> Copyright 2014, Springer Nature. B) Diagram showing the single-electron excitations and the effect of size, shape, and material on hot electron generation. Reproduced with permission.<sup>[83]</sup> Copyright 2017, American Chemical Society. C) The quality factors for selected refractory materials in comparison with those of Au and Ag. Reproduced with permission.<sup>[86]</sup> Copyright 2016, American Chemical Society. D) Summary of the favorable type of hot carriers for extraction in various metals, alloys, and nanostructures. Reproduced with permission.<sup>[82]</sup> Copyright 2019, Wiley-VCH.

compared to that in an oxide-free system. The photocurrent enhancement is universal and appropriate for the device of p-Si with various other metals such as Au and Ti. Besides the conventional hot electron transfer mechanism in three steps: hot electron generation, transport, and emission processes, the novel hot-electron transfer by a plasmon-induced interfacial charge-transfer transition in synthesized cadmium selenide quantum dot (QD)-Au dimers has been investigated recently.<sup>[50]</sup> By the excitation of surface plasmons, electrons and holes are directly generated in the conduction bands of semiconductor and metal as shown in Figure 13C. The quantum efficiency has been demonstrated to be up to 24%, which is independent of the incident photon energy.

#### 4.2. Hot Carrier Engineering with New Plasmonic Materials

Noble metals such as Au and Ag are among the most popular plasmonic materials and have been intensively explored in hot carrier excitation and extraction due to the high carrier concentration and large negative permittivity. However, the plasmonic resonances normally occur in a narrow visible band and complex nanostructures are usually required to broaden the resonances

and shift the resonance to NIR.<sup>[80]</sup> In addition, considering hot carrier extraction, the Schottky barrier height is usually too high to collect low-energy hot carriers due to the large work function, e.g., 5.1 eV for Au.<sup>[81]</sup> The last but not least, noble metals are expensive and scarce, preventing them from large-scale practical application.<sup>[82]</sup> Thus, to expand the alternative materials and investigate their potential for hot-carrier excitation, it is worth exploring the new plasmonic materials for generating and collecting hot carriers.

**Figure 14A** shows the calculated optical extinction of noble material nanoparticles (e.g., Au, Ag, Cu, and Al) and conducting oxide.<sup>[8]</sup> The optical absorption of noble metallic nanoparticles is very intensive and narrow in the short wavelength region of the visible band, which however is not appropriate for infrared hot carrier photodetection. While the conducting oxides have broader absorptions than noble metals in the infrared, which is beneficial for broadband hot carrier photodetection in the infrared. Furthermore, the carrier concentration of conducting oxide can be tuned by changing the doping concentration to control the spectral band of plasmonic resonance, as shown by aluminum doped zinc oxide (AZO). For the efficient hot carrier injection, the alignment of the Fermi level of the plasmonic materials with

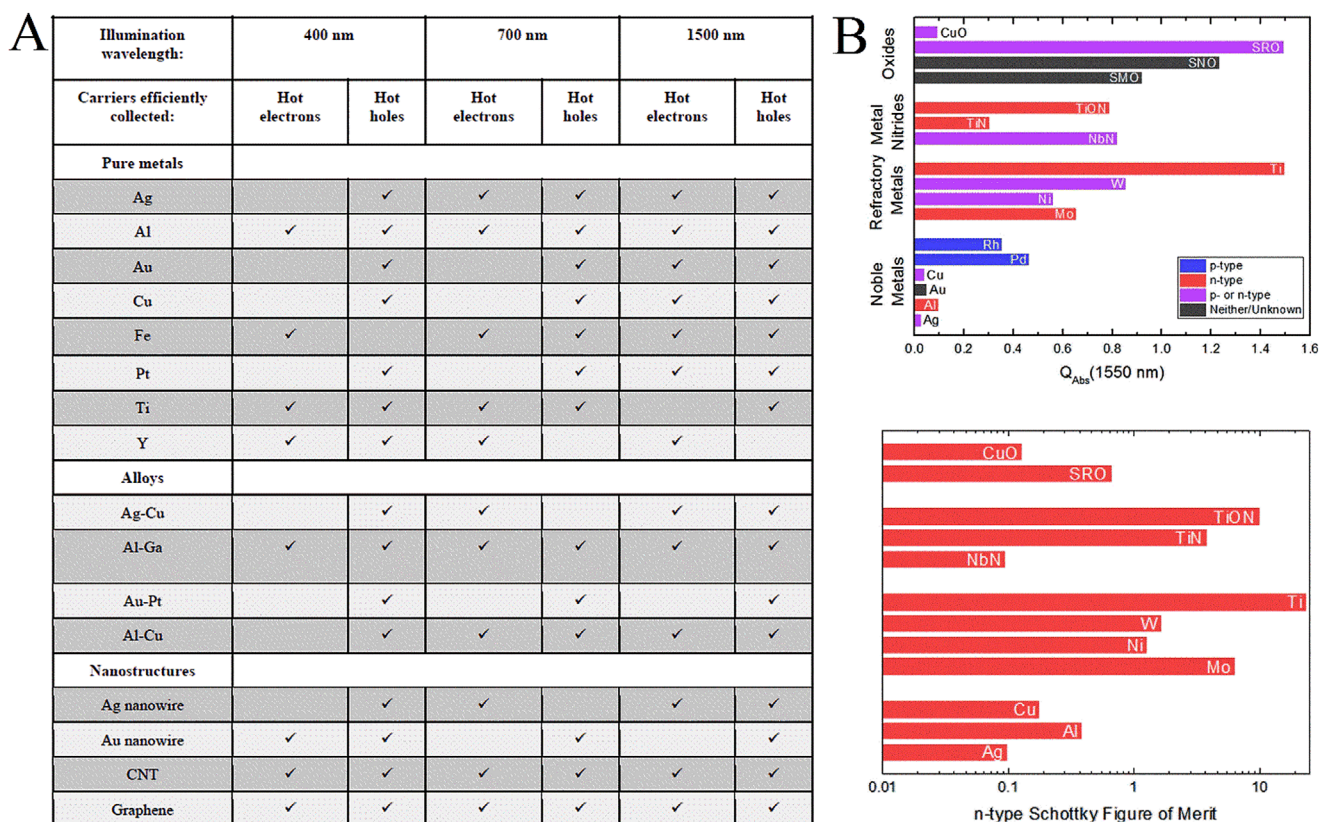


**Figure 15.** A) Summary of the preferred hot carrier type for collection in the noble metals, transition metal nitride, transition metal carbide, and metal oxide. Reproduced with permission.<sup>[73]</sup> Copyright 2015, OSA Publishing. B) The optimized optical cross-sections (top panel) and the overall photodetection efficiency (bottom panel) comparisons for n-type Schottky contact at the wavelength of 1550 nm. Reproduced with permission.<sup>[87]</sup> Copyright 2019, American Chemical Society.

semiconductors is important.<sup>[8]</sup> Figure 14A shows that the Fermi energy level is around 0 V on the normal hydrogen electrode scale for noble metals and conducting oxides. Recently, a theory based on quantum and classical mechanisms is developed to describe the hot electron generation rates and initial energy distributions in nanocrystals with various geometries.<sup>[83]</sup> Figure 14B shows that the size, shape, and material play a crucial role in hot electron generation efficiency in a nanocrystal. The energy efficiency of creating high-energy hot electrons in nanocrystals with nanosphere and nanorod shapes is determined by the ratio of mean free path and size. Thus, small sizes of nanocrystals with a long mean free path are an advantage for the hot electron generation rate. Besides, the generation efficiency increases strongly with complex shapes and hot spots, such as nanostars, nanocubes, and metamaterial absorbers with gap plasmons.<sup>[84,85]</sup> Recently, first-principles density functional theory (DFT) calculations and a systematic quantitative method have been performed to survey the promising plasmonic materials for hot-carrier applications including the noble metals, refractory materials [titanium carbide (TiC), zirconium carbide (ZrC), hafnium carbide (HfC), tantalum carbide (TaC), tungsten carbide (WC), TiN, zirconium nitride (ZrN), hafnium nitride (HfN), tantalum nitride (TaN), and tungsten nitride (WN)], transition metal nitrides, and conductive oxides.<sup>[86,87]</sup> It is confirmed from Figure 14C that transition metal nitrides, such as TiN, ZrN, and HfN, have comparable perfor-

mance to noble metals in the visible to near-infrared regions. By simultaneously considering the optical absorption in plasmonic materials and hot carrier injection efficiency, the materials of molybdenum (Mo), titanium (Ti), TiN, and titanium oxynitride (TiON) [(Pd) have the highest figure-of-merit in photodetection at 1550 nm due to the low-height Schottky barrier formed with n-Si [p-Si]. Figure 14D summarizes the main properties of the transition metal nitrides, transition metal carbides, and metal oxides in comparison to gold and silver.<sup>[82]</sup> It is noted that the working wavelength and plasmon resonance are obtained under the assumption of highly symmetric single nanoparticles. The noble metallic particles have narrowband resonances in the visible, while nonmetallic nanoparticles can have broadband plasmon resonances from visible to NIR. Some nonmetallic materials can have higher efficiencies than the conventional noble metals in hot carrier applications including photoelectric or photothermal conversions. In addition, the nonmetallic materials are usually cheaper (except the highly expensive transition metals used) than the noble metals, which is beneficial for large-scale practical hot carrier applications.

According to the hot carrier energy distributions based on the electron density of states, **Figure 15A** summarizes the preferred carrier type for excitation and extraction in the plasmonic materials, ranging from pure metals and alloys to nanowires and graphene across the visible to infrared band.<sup>[73]</sup> Under specific il-

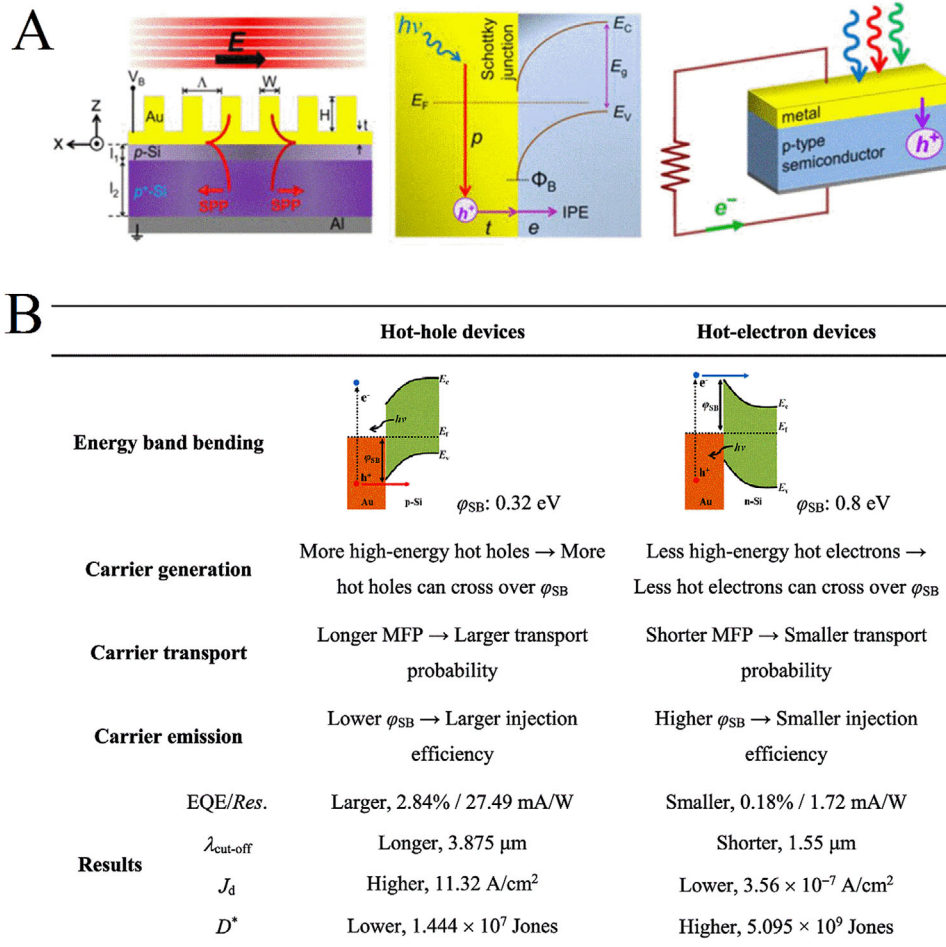


**Figure 16.** A) Cross-sectional sketch, energy band diagram, and internal photoemission process of the Au/Si hot hole photodetector consisting of a metallic grating and a thin metal patch on silicon. Reproduced with permission.<sup>[89]</sup> Copyright 2016, OSA Publishing. B) Summary of the physical difference and the performance comparison between the hot hole and hot-electron photodetectors. Reproduced with permission.<sup>[88]</sup> Copyright 2019, American Chemical Society.

lumination conditions, different plasmonic materials should be chosen by considering hot carrier energy distributions. The design principles provide rough guidance for the choice of appropriate hot carrier type to collect and show many potential materials for hot-carrier plasmonic devices, apart from the traditional noble metals. To systematically investigate the suitability of materials for hot-carrier photodetection, the overall photodetection efficiency is quantified from the fundamental electronic and optical properties of each material, by considering the operation of the embedded sphere in the Si.<sup>[87]</sup> The photodetection efficiency is the multiple of the hot carrier excitation efficiency and the injection probability, which are respectively obtained by Mie theory and the modified Fowler yield. Figure 15B illustrates the optimized absorption cross-sections (top panel) and the overall photodetection efficiency for n-type Schottky contact (bottom panel) under the illumination wavelength of 1550 nm based on the four material classes, including the noble metals, refractory metals, transition metal nitrides, and conductive oxides. It is found that the Schottky barrier height plays a key role in selecting appropriate materials and Mo, Ti, TiN, and TiON have the highest figure of merit values due to the low barrier with n-Si.

### 4.3. Hot Carrier Engineering with Other Approaches

Hot carrier photodetectors are drawing significant attention due to the above-mentioned advantages; nevertheless, most of the research focuses on how to extract hot electrons based on conventional noble metals (e.g., Au, Ag) and semiconductors (e.g., Si, TiO<sub>2</sub>). To further improve the performance of hot carrier photodetectors, a number of new physical mechanisms have been explored, including the extraction of hot holes, 2D materials, and perovskites.

Normally, the Schottky barriers formed by noble metals and p-Si are lower than those with n-Si.<sup>[88]</sup> Thus, hot hole photodetectors can have a higher photoconversion efficiency and a wider spectral region than that of hot-electron devices. For example, the plasmonic Schottky photodetector in **Figure 16A** consisting of metallic gratings and patch on p-Si has a barrier height of 0.32 eV, much lower than that of hot electron device (0.8 eV). The incident light is coupled perpendicularly to SPPs propagating along with the thin metal patch, leading to the generation of hot holes near the Schottky interface.<sup>[89]</sup> As a result, the responsivity is  $\approx 13 \text{ mA W}^{-1}$  at 1550 nm under a low reverse bias, among the highest

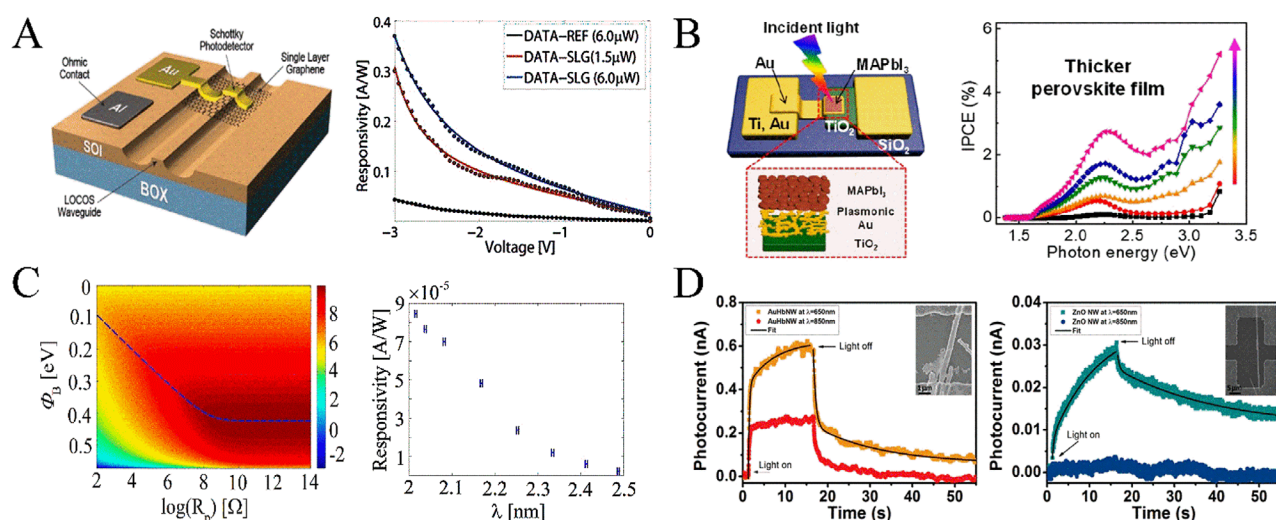


**Figure 17.** A) Schematic diagram and the responsivity versus voltage of the metal graphene–silicon plasmonic Schottky photodetector coupled to Si waveguide. Reproduced with permission.<sup>[95]</sup> Copyright 2016, American Chemical Society. B) Schematic and IPCE spectra of the perovskite plasmonic nanodiode. The active area of MAPbI<sub>3</sub>/plasmonic-Au/TiO<sub>2</sub> is magnified. Reproduced with permission.<sup>[96]</sup> Copyright 2019, American Chemical Society. C) SNR as a function of the Schottky barrier and shunt resistance; the measured responsivity of the hot carrier photodetector based on Al/Si pyramids. Reproduced with permission.<sup>[97]</sup> Copyright 2017, American Chemical Society. D) Photoresponse of the hybrid Au nanorods–ZnO nanowire (left) and bare ZnO photodetectors under the light incidence of  $\lambda = 650$  and 850 nm. Reproduced with permission.<sup>[98]</sup> Copyright 2014, American Chemical Society.

values reported to date for sub-bandgap detectors based on internal photoemission. To guide designing high-performance hot carrier photodetectors, the comprehensive comparison has been summarized in Figure 16B regarding the energy band bending, initial energy distribution, transport, and interfacial emission efficiency in hot hole and electron generation, transport, and emission processes.<sup>[88]</sup> Taking the typical Au/Si Schottky contact as an example, hot hole devices have a larger fraction of high-energy hot carriers after excitation, a higher transport, and injection efficiency due to the larger MFP and lower barrier height. Therefore, hot hole devices have advantages in responsivity and long-wavelength photodetection.

The outstanding characteristics of graphene and other 2D materials make them attractive for photonics and optoelectronic applications.<sup>[90–92]</sup> The ultrafast carrier dynamics, broadband absorption, tunable optical property, and high electron mobility enable ultrafast, broadband, and ultrasensitive photodetection.<sup>[93,94]</sup> By integration with the internal photoemission process, the performance of hot carrier photodetectors could be potentially promoted. A graphene-integrated hot-electron photodetector in a waveguide has been reported as shown in Figure 17A.<sup>[95]</sup> It is found that the integration of single-layer graphene improves the responsivity to 85 mA W<sup>-1</sup> with the corresponding IQE of 7% at 1550 nm, which is one order of magnitude enhanced compared to that without single-layer graphene. Under a reverse bias of 3 V, the responsivity can be further increased up to  $\approx 0.37$  A W<sup>-1</sup> with the corresponding photogain of  $\approx 2$ . This responsivity is the highest among the reported waveguide-integrated Si-based photodetectors and is even comparable to state-of-the-art SiGe devices. The lifetime of hot electrons is a key factor to determine the photoelectric conversion efficiency. It is found from Figure 17B that the deposition of perovskite (MAPbI<sub>3</sub>) layers on plasmonic Au/TiO<sub>2</sub> Schottky junction can considerably improve hot electron generation by the effective light absorption from

the enhanced near-field in plasmonic Au.<sup>[96]</sup> The improved hot-electron flux in MAPbI<sub>3</sub> and the efficient capture of hot electrons via the formation of a 3D Schottky interface contribute to an improved photocurrent. The femtosecond transient absorption spectroscopy confirmed that the hot electrons in MAPbI<sub>3</sub> have a longer lifetime of 62.38 ps, which is  $\approx 22$  times longer compared to that of hot electrons in Au.

The above discussions focus on the thermodynamic loss analysis and the strategies to improve the responsivity of hot carrier photodetectors. Here, we concentrate on the detailed analysis for the optimization in terms of the figure of merits such as signal-to-noise ratio (SNR) and noise equivalent power (NEP). With a quantitative estimation of various noise mechanisms including the background noise, Johnson noise, shot noise of the optical signal, and the shot noise of dark current, it is found that the dark current noise dominates the noise sources in hot carrier photodetectors.<sup>[97]</sup> Figure 17C plots SNR as a function of Schottky barrier height in an ideal hot carrier photodetector. The optimal Schottky barrier height for achieving the highest SNR is  $h\nu - \frac{4kT}{e}$ , where  $h$  is the Planck constant,  $\nu$  is the optical frequency,  $k$  is the Boltzmann's constant,  $T$  is the temperature, and  $e$  is the electron charge. The SNR is relatively high in the case of high shunt resistance and is mainly limited by the large dark current (low photocurrent) under a low (high) Schottky barrier. In the case of low shunt resistance, the SNR is relatively small and the optimal Schottky barrier height decreases with increasing the shunt resistance. Based on a low Schottky barrier height of 0.48 eV formed in the contact of Al and Si, Figure 17C shows that the fabricated hot carrier photodetectors have a wide spectral response up to  $\approx 2.5$   $\mu\text{m}$  with NEP in the range of  $10^{-8}$  [ $\frac{\text{W}}{\sqrt{\text{Hz}}}$ ] or even below. Since the hot carrier relaxation time is on the order of the femtosecond scale, the hot carrier photodetectors could have a significant advantage in ultrafast response. The response time of a full device is also strongly dependent

on the local field enhancement of the plasmonic geometry.<sup>[30]</sup> It is found from Figure 17D that the response speed of the Au nanorod–ZnO nanowire hybrid hot carrier photodetector is more than one order of magnitude faster than the bare ZnO semiconductor photodetector.<sup>[98]</sup> In addition, it is demonstrated that in the Au nanoantenna/molybdenum disulfide (MoS<sub>2</sub>) heterostructures, the hot electrons are transferred from Au to MoS<sub>2</sub> on the order of 200 fs, which indicates an ultrafast optical response time and a high cutoff frequency.<sup>[99]</sup>

#### 4.4. Hot Carrier Novel Functionalities

In this section, we present a brief introduction regarding the novel functionalities of hot carrier photodetectors. In addition to the advantages of below-bandgap photodetection, room-temperature operation, high tunability of working wavelength, the novel functionalities of hot carrier photodetectors such as nanoscopy, circularly polarized light detection, ultrasensitive optoelectronic sensing, wavelength detector, all-optical/photocapacitance modulation, and transistors have been widely explored.<sup>[100–109]</sup> For hot-electron nanoscopy, a plasmonic nanotaper in contact with semiconductor in Figure 18A is used to adiabatically compress and efficiently transform the SPPs into hot electrons to enable a high hot-electron conversion efficiency.<sup>[100]</sup> Then, by the integration of an atomic force microscopy setup, the local chemical sensitivity of the semiconductor surface is obtained from the hot electron photocurrent map by scanning the taper on the semiconductor. For the circularly polarized light detector, the chiral plasmonic metamaterials in Figure 18B are engineered to perfectly absorb specific circular polarized light while reflecting the complementary component.<sup>[101]</sup> Then, by placing the metallic nanostructure in contact with Si, the left and right hand circularly polarized light can be distinguished from the hot electron photocurrent without the use of additional optical elements. The optoelectronic sensing with a direct electrical read-out capability is demonstrated in Figure 18C by combining the narrowband resonant absorption in the plasmonic nanotrench arrays with hot electron injection.<sup>[102]</sup> The resultant narrowband responsivity peak is sensitive to the environmental refractive index, enabling a high sensitivity of 3017 mA W<sup>-1</sup> RIU<sup>-1</sup>. For wavelength detector, it is demonstrated in Figure 18D that the open-circuit voltage in the MIM diode is independent of incident power and directly proportional to the energy difference between the incident photon and the electron barrier.<sup>[103]</sup> Thus, the open-circuit voltage varies monotonically with photon energy and realizes the monochromatic wavelength determination and real-time polychromatic deconvolution with a single easily fabricated MIM device.

For spectrally selective photocapacitance modulation in Figure 18E, the plasmonic nanochannel structure excites surface plasmons, focuses, and confines light at the Schottky interfaces, leading to a narrowband optical resonance and the generation of a number of hot electrons.<sup>[109]</sup> The accumulated hot electrons change the electrical impedance of the structure, offering a practical means of monitoring changes of photocapacitance induced by the near field. Another way to realize the spectral-selective plasmonic monitoring is to use the channel-coupled nanogap structure consisting of highly doped semiconductor channels

and metal slabs, as shown in Figure 18F. The photoabsorption in the semiconducting channel results in a decrease in the Schottky barrier height. Under light illumination of transverse magnetic (TM) polarization, light is confined to the Schottky interfaces by the excitation of surface plasmons, which increases the generation of hot carriers and decreases photoabsorption in the semiconducting channel. In this case, the reduced photoabsorption results in a decreased photoconductivity and a strong impedance change relative to that under transverse electric (TE) incidence.<sup>[108]</sup> Thus, the channel-coupled nanogap structure can be used as a plasmonic monitor for nano/micro devices. Recently, all-optical-input transistors are realized in a plasmonic porous Ag/TiO<sub>2</sub> structure (Figure 18G).<sup>[104]</sup> A near-infrared light of 980 nm is used as the source light to excite surface plasmons in the porous Ag layer, generate hot electrons and form a photocurrent. Ultraviolet light of 365 nm is used as the gate light to tune the height of the Ag/TiO<sub>2</sub> Schottky barrier via the internal photoelectric effect in the porous TiO<sub>2</sub>. As a result, the hot electron photocurrent by the source light can be improved by more than 100 times by controlling the gate light. Another type of plasmon field-effect transistor consists of a heavily doped n-type Si substrate, an n-type ZnO film on thermally grown SiO<sub>2</sub>, and gold nanoparticles (Figure 18H).<sup>[107]</sup> The localized surface plasmons are excited in the gold nanoparticles, decayed into hot electrons, and inject over the Schottky barrier into ZnO film, resulting in an increased channel conductivity and drain current. With a gate voltage bias to control the internal electric field and quantum tunneling effect, the responsivity can be amplified to more than 3 A W<sup>-1</sup>. Furthermore, it has been demonstrated that the femtosecond all-optical modulation can be realized in the plasmonic system of a square array of Au nanocubes on an Au film separated by a 10 nm thick ITO spacer (Figure 18I).<sup>[105]</sup> The extraction of plasmonic hot electrons from Au nanocubes triggers an electron-dominated relaxation channel, which allows the equilibration of optically excited plasmonic systems to occur within a timescale shorter than 200 fs. The relaxation kinetics and the optical nonlinearity can be controlled by the spectral response of the plasmonic design.

## 5. Conclusions and Outlook

In conclusion, we have reviewed the recent progress of hot carrier photodetectors working from ultraviolet to infrared regime, ranging from hot carrier dynamics, nanostructured/planar hot carrier photodetectors to potential strategies for enhanced performance and novel functionalities. The generated hot carrier energy distribution is strongly dependent on the material, size, shape, and incident photon energy.<sup>[83,84]</sup> High-energy hot carriers are more generated in small nanoparticles with complex shapes and enhanced electric fields. The electronic band structure plays a key role in hot carrier energy and momentum distribution (for interband transition under excitation of high-energy photons). The hot carrier transport behavior is investigated from theory (Boltzmann analysis, Monte Carlo method, and dual-temperature model) and experiment via ultrafast pump-probe measurement.<sup>[10]</sup>

Finally, we make a comprehensive comparison of the reported hot carrier photodetectors including the responsivity, dark current, detectivity, and NEP in Table 1. Hot carrier photodetec-

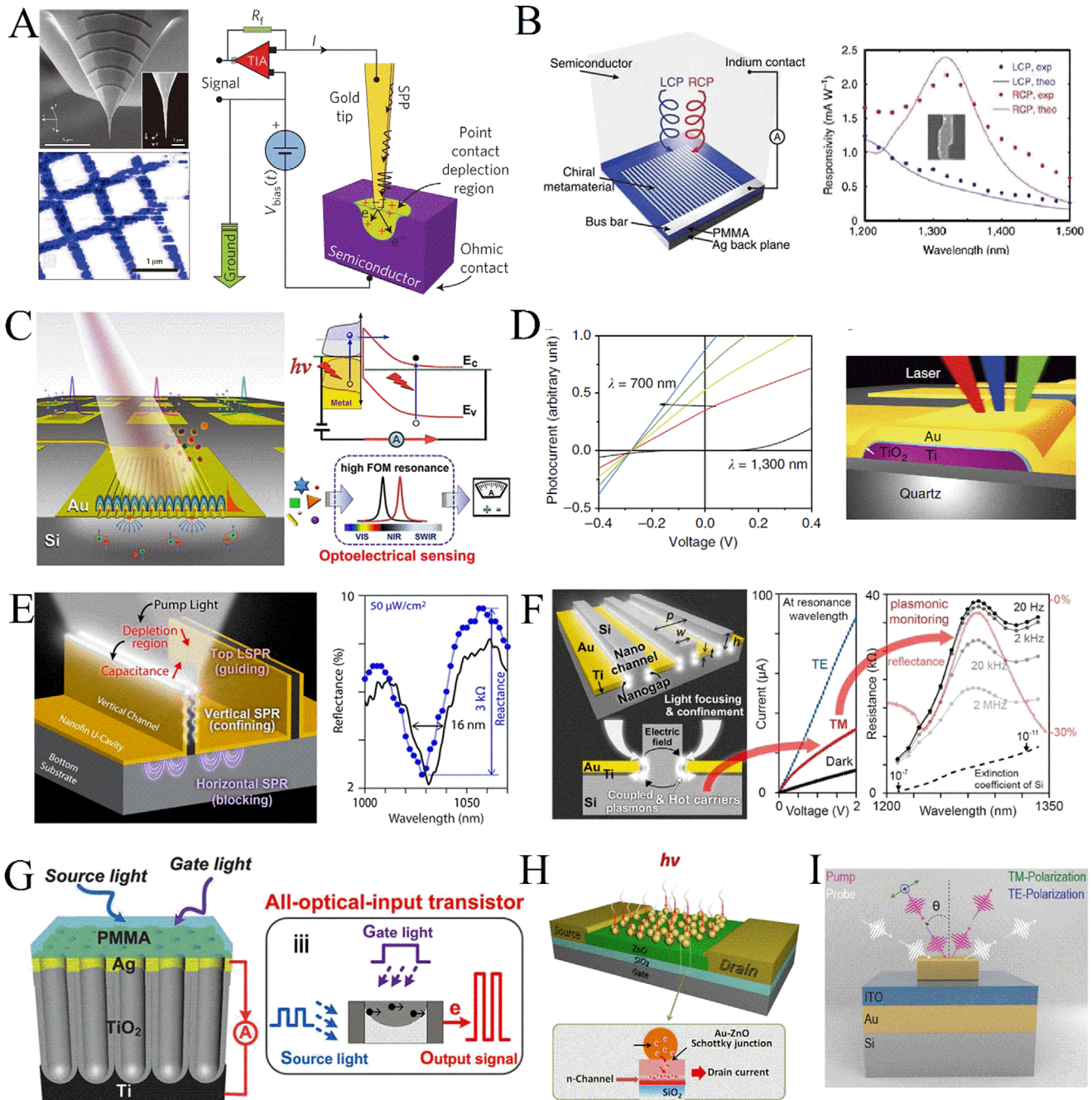


**Figure 18.** A) SEM of the nanotaper, hot electron photocurrent map generated by the nanotaper, and the schematic of hot electron nanoscopy. Reproduced with permission.<sup>[100]</sup> Copyright 2013, Springer Nature. B) Left: schematic of the circularly polarized light detector consisting of a chiral metamaterial integrated with a semiconductor. Right: experimentally measured (dots) and theoretically calculated (solid curve) responsivity spectra under left (right)-handed circularly polarized illumination. Reproduced with permission.<sup>[101]</sup> Copyright 2015, Springer Nature. C) Schematic of the refractive index sensor with direct electrical readout. Reproduced with permission.<sup>[102]</sup> Copyright 2019, American Chemical Society. D) Schematic of the wavelength detector in a MIM diode and the photocurrent as a function of bias under various light illumination. Reproduced with permission.<sup>[103]</sup> Copyright 2013, Springer Nature. E) Schematic diagram, reflectance spectrum, and reactance variations versus incident light wavelength of the readable photocapacitor based on a plasmonic nanochannel structure. Reproduced with permission.<sup>[109]</sup> Copyright 2016, American Chemical Society. F) Schematic diagram, current–voltage characteristics, and resistance variations versus TM-polarized incident light wavelength in the channel-coupled nanogap structure. Reproduced with permission.<sup>[108]</sup> Copyright 2018, American Chemical Society. G) Schematic of the all-optical-input transistor. Reproduced with permission.<sup>[104]</sup> Copyright 2018, Wiley-VCH. H) Schematic diagram and the operational principle of the plasmon field-effect transistor. Reproduced with permission.<sup>[107]</sup> Copyright 2016, American Chemical Society. I) Schematic of the hot-electron-assisted femtosecond all-optical modulation. Reproduced with permission.<sup>[105]</sup> Copyright 2018, Wiley-VCH.

**Table 1.** Summary of reported hot carrier photodetectors from ultraviolet to infrared. (Notes: under no bias unless specified).

Device	Device type	Responsivity	Spectral range	Dark current/dark current density	Detectivity [Jones]	NEP [ $W/\sqrt{Hz}$ ]
Lin et al. <sup>[115]</sup>	Graphene/ $\beta$ -Ga <sub>2</sub> O <sub>3</sub>	12.8 A W <sup>-1</sup> @254 nm (-6 V)	UV	$1.25 \times 10^{-8}$ A cm <sup>-2</sup>	$1.30 \times 10^{13}$	NA
Wang et al. <sup>[21]</sup>	Sn nanodots/ SiO <sub>2</sub> /n-Si	29.3 mA W <sup>-1</sup> @269 nm (4 V)	UV	$1 \times 10^{-10}$ A	$1 \times 10^{11}$	$1.93 \times 10^{-13}$
Ahmadivand et al. <sup>[116]</sup>	Al heptamer antennas/GaN	21.9 A W <sup>-1</sup> @325 nm (5 V)	UV	$5.5 \times 10^{-8}$ A (5 V)	NA	$6.08 \times 10^{-15}$ (5 V)
Gong et al. <sup>[117]</sup>	Planar Al/Al <sub>2</sub> O <sub>3</sub> /ITO	240 nA W <sup>-1</sup> @420 nm	Visible	NA	NA	NA
Chalabi et al. <sup>[22]</sup>	Antenna Au/Al <sub>2</sub> O <sub>3</sub> /Au	250 nA W <sup>-1</sup> @400 nm	Visible	NA	NA	NA
Wang et al. <sup>[118]</sup>	Au/Al <sub>2</sub> O <sub>3</sub> /Au with prism	10 nA W <sup>-1</sup> @633 nm	Visible	NA	NA	NA
Gong et al. <sup>[62]</sup>	Planar Au/Al <sub>2</sub> O <sub>3</sub> /ITO	45 nA W <sup>-1</sup> @500 nm 5 nA W <sup>-1</sup> @700 nm	Visible	NA	NA	NA
Lee et al. <sup>[52]</sup>	Ag islands/TiO <sub>2</sub>	8.9 mA W <sup>-1</sup> @459 nm	Visible	$1 \times 10^{-8}$ A	$3.14 \times 10^{10}$	$6.36 \times 10^{-12}$
Arquer et al. <sup>[24]</sup>	Plasmonic crystal Au/TiO <sub>2</sub> /ITO	70 mA W <sup>-1</sup> @640 nm (4 V)	Visible–NIR	$3 \times 10^{-11}$ A	NA	NA
Elabd et al. <sup>[119]</sup>	Thin-film PtSi/Si	0.2 A W <sup>-1</sup> @1500 nm	LW-NIR	NA	NA	NA
Sobhani et al. <sup>[6]</sup>	Au grating/Si	0.6 mA W <sup>-1</sup> @1460 nm	LW-NIR	NA	NA	NA
Li et al. <sup>[56]</sup>	Metamaterial Au/Si	3 mA W <sup>-1</sup> @1300 nm	LW-NIR	NA	NA	NA
Desiatov et al. <sup>[57]</sup>	Al/Si pyramids	12 mA W <sup>-1</sup> @1300 nm 5 mA W <sup>-1</sup> @1550 nm	NIR	$1 \times 10^{-7}$ A	NA	$1.49 \times 10^{-11}$ $3.58 \times 10^{-11}$
Knight et al. <sup>[76]</sup>	Au NWs embedded in Si	0.065 mA W <sup>-1</sup> @1500 nm	LW-NIR	$1 \times 10^{-9}$ A	$3.63 \times 10^6$	$2.75 \times 10^{-10}$
Knight et al. <sup>[13]</sup>	Nanoantennas Au/Si	10 $\mu$ A W <sup>-1</sup> @1250 nm 3 $\mu$ A W <sup>-1</sup> @1550 nm	LW-NIR	NA	NA	NA
Lin et al. <sup>[58]</sup>	Deep-trench/thin Au/Si antenna	3 mA W <sup>-1</sup> @1300 nm 1.25 mA W <sup>-1</sup> @1400 nm 0.5 mA W <sup>-1</sup> @1550 nm	LW-NIR	$8.7 \times 10^{-9}$ A cm <sup>-2</sup>	$5.68 \times 10^{10}$ $2.37 \times 10^{10}$ $9.47 \times 10^9$	NA
Feng et al. <sup>[112]</sup>	Metasurface Au/Si	94.5 mA W <sup>-1</sup> @1150 nm (1.5 V)	LW-NIR	$1.45 \times 10^{-7}$ A cm <sup>-2</sup>	$4.38 \times 10^{11}$	NA
Grajower et al. <sup>[97]</sup>	Al/Si pyramid	$5 \times 10^{-5}$ A W <sup>-1</sup> @2150 nm (0.8 V)	LW-NIR	$1 \times 10^{-10}$ A	$2.82 \times 10^5$	$3.14 \times 10^{-10}$
Nicholas et al. <sup>[79]</sup>	Thin film TiN/p-Si	1 mA W <sup>-1</sup> @1250 nm	LW-NIR	$3 \times 10^{-10}$ A	$6.12 \times 10^8$	$9.8 \times 10^{-12}$
Tanzid et al. <sup>[59]</sup>	Au grating/p-Si	1 A W <sup>-1</sup> @1375 nm (275 mV)	LW-NIR	NA	$1.63 \times 10^8$	$9.23 \times 10^{-12}$
	Pd grating/p-Si	1 A W <sup>-1</sup> @1375 nm (93 mV)	LW-NIR		$1.63 \times 10^8$	$8.05 \times 10^{-12}$
Krayer et al. <sup>[55]</sup>	Thin film Pt/Si	$10^{-4}$ – $10^{-6}$ A W <sup>-1</sup> @1200–1500 nm	LW-NIR	$4 \times 10^{-8}$ A cm <sup>-2</sup>	60–2000	NA
Krayer et al. <sup>[120]</sup>	Au and Ag alloys/n-Si	$2 \times 10^{-5}$ – $4 \times 10^{-4}$ A W <sup>-1</sup> @1200–1600 nm	LW-NIR	NA	NA	NA
Casalino et al. <sup>[121]</sup>	Waveguide Cu/p-Si	0.08 mA W <sup>-1</sup> @1550 nm (-1 V)	LW-NIR	$1.7 \times 10^{-8}$ A (-1 V)	NA	$9.23 \times 10^{-10}$
Wen et al. <sup>[61]</sup>	Disordered Au Si NHs	1.5–13 mA W <sup>-1</sup> @1100–1500 nm	LW-NIR	$1 \times 10^{-6}$ A	NA	$4.75 \times 10^{-11}$ – $3.77 \times 10^{-10}$
Wen et al. <sup>[60]</sup>	Au NPs in Si/TiO <sub>2</sub>	3.3 mA W <sup>-1</sup> @1500 nm (-5 V)	LW-NIR	NA	NA	NA
Lin et al. <sup>[72]</sup>	Deep-trench/thin-metal Ni/Si antenna	0.33 mA W <sup>-1</sup> @1550 nm 0.2 mA W <sup>-1</sup> @1750 nm	LW-NIR	NA	NA	NA
Yang et al. <sup>[122]</sup>	Au/Si NWs	2.5 mA W <sup>-1</sup> @1310 nm	LW-NIR	$4 \times 10^{-8}$ A	NA	$4.53 \times 10^{-11}$

(Continued)



**Table 1.** (Continued).

Device	Device type	Responsivity	Spectral range	Dark current/dark current density	Detectivity [Jones]	NEP [W/√Hz]
Wang et al. <sup>[123]</sup>	Au NWs/bilayer MoS <sub>2</sub>	5.2 A W <sup>-1</sup> @ 1070 nm (0.8 V)	NIR	NA	NA	NA
Goykhman et al. <sup>[95]</sup>	On-chip integrated Au/graphene/Si	85 mA W <sup>-1</sup> @ 1550 nm (1 V) 0.37 A W <sup>-1</sup> @ 1550 nm (3 V)	LW-NIR	2 × 10 <sup>-8</sup> A	NA	1.1 × 10 <sup>-12</sup>
Goykhman et al. <sup>[77]</sup>	Waveguide-based Al/Si	12.5 mA W <sup>-1</sup> @ 1550 nm (0.1 V)	LW-NIR	3 × 10 <sup>-8</sup> A (0.1 V)	NA	7.84 × 10 <sup>-12</sup> (0.1 V)
Goykhman et al. <sup>[124]</sup>	Nanoscale Au/Si waveguide	13.3 mA W <sup>-1</sup> @ 1310 nm (0.1 V) 0.25 mA W <sup>-1</sup> @ 1550 nm (0.1 V)	LW-NIR	1.3 × 10 <sup>-8</sup> A (0.1 V)	NA	4.82 × 10 <sup>-12</sup> 2.58 × 10 <sup>-10</sup>
Akbari et al. <sup>[125]</sup>	Au stripe/p-Si	15.2 mA W <sup>-1</sup> @ 1310 nm	LW-NIR	5.59 × 10 <sup>-6</sup> A	1.14 × 10 <sup>7</sup>	8.8 × 10 <sup>-11</sup>
Akbari et al. <sup>[126]</sup>	SP waveguide Au/Si	0.38 mA W <sup>-1</sup> @ 1280 nm	LW-NIR	1 × 10 <sup>-8</sup> A	3.49 × 10 <sup>7</sup>	1.49 × 10 <sup>-10</sup>
	SP waveguide Al/Si @ 1310 nm	1.04 mA W <sup>-1</sup>	LW-NIR	6 × 10 <sup>-6</sup> A	7.53 × 10 <sup>6</sup>	1.33 × 10 <sup>-9</sup>
Muehlbrandt et al. <sup>[127]</sup>	Waveguide Au/Si	0.12 A W <sup>-1</sup> @ 1550 nm (3.25 V)	LW-NIR	2 × 10 <sup>-5</sup> A (3.25 V)	NA	NA

tors are mainly investigated for operation in the LW-NIR regime, beyond the limit of conventional Si-based photodetectors. The working spectral range can be easily tuned from UV, visible to NIR via adjusting the materials that form the junction. The main drawback of hot carrier photodetectors is the low responsivity due to the limited high-energy generation rate, ultrafast thermalization, and momentum mismatch in the interfacial electron transfer process.<sup>[10,30,69]</sup> Therefore, the various metallic nanostructures including nanodots, antennas, metamaterials, islands, plasmonic crystals, grating, and waveguide are employed to excite SP for an improved responsivity.<sup>[6,22,24,51,57,110-127]</sup> In general, the unbiased responsivities of the hot carrier photodetectors working at the LW-NIR are on the order of mA/W, much lower than that of the commercially available near-infrared photodetectors, e.g., indium arsenide (InAs), gallium arsenide (GaAs), and mercury cadmium telluride (HgCdTe).<sup>[112]</sup> To further improve the efficiency of hot carrier photodetectors, more works can be interesting from the following perspectives.

1) A fundamental understanding of the hot carrier mechanisms through ultrafast transient absorption spectroscopy assisted by the first-principles calculations. To guide the design of high-performance hot carrier photodetectors, a complete microscopic understanding of the hot carrier photoconversion dynamics in real devices is necessary. Due to the large variation of the length scales in devices from the atomic to the mesoscale, the classical electromagnetic simulations and the theoretical description of the hot carrier generation are challenging since the quantum effects should be considered for small nanostructures.<sup>[10]</sup> On the other hand, the time scales from hot carrier thermalization to equilibration with lattice rang from a few femtoseconds to picoseconds regime, which makes the direct measurement of the spatial and temporal evolution of hot carrier energy and momentum distributions challenging. The breakthrough in the above two aspects could facilitate the study of hot carrier photodetectors.

2) Novel metallic nanostructures to facilitate the high-energy hot carrier generation and interface engineering for an efficient hot carrier extraction, such as a strong-coupling regime between excitonic and plasmonic resonances. An essential challenge lies in developing a plasmonic nanostructure (including the size, shape, and material) with an enhanced concentrated electric field and perfect optical absorption in ultrathin or small nanostructures to simultaneously improve the efficiency of hot carrier generation, transport, and collection performances. For a practical photodetection technology, the fabrication of the complicated metallic nanostructures is still challenging and simple and low-cost fabrication is required. Therefore, the planar scenarios for cost-effective strategies are worth to be considered with a delicately designed configuration.

3) New plasmonic materials with a high electron density near the Fermi level and a long carrier lifetime such as ceramics and metal alloys. For alloys, the electron density of states can be flexibly engineered by controlling the compositions and crystallographic orientations. The hot carrier lifetime, generation efficiency, and initial energy distribution can be more favorable for extraction compared to that in constituent metals. Some nonmetallic materials such as transition metal nitrides/carbides/borides show plasmonic resonances with metallic band structures.<sup>[82]</sup> Compared to the conventional metals, the hot carrier mean free paths in these nonmetallic materials can be longer; the Schottky barrier heights formed with the semiconductors can be lower; the plasmonic response can be broad and tunable. In addition, they are abundant and cost-effective, which is beneficial for large-area practical applications. Due to the high electron mobility, tunable optical and electrical properties, ultrafast carrier dynamics, and long momentum relaxation times such as graphene, molybdenum disulfide, and phosphorene, 2D materials are attractive for hot carrier photodetectors.<sup>[113]</sup> The limited light-matter interaction in 2D materials arising from the atomic thickness can be promoted by exciting surface plasmons to con-

centrate electric field. The hot carrier injection combined with 2D materials is an appealing direction for high-performance photodetection.

In this respect, the first-principles calculations can be conducted to comprehensively study the electronic band structure, dielectric function to pick the potential materials.<sup>[114]</sup> On the other hand, more functionalities of hot carrier photodetectors can be explored from the all-silicon photonic chip, infrared sensing, communication, etc. The hot carrier photodetectors with high efficiencies and enormous practical applications are worth of expectation in the future.

## Acknowledgements

This work was supported by the National Natural Science Foundation of China (61875143, 61905170, and 62120106001), Natural Science Foundation of Jiangsu Province (BK20190816), Suzhou Science and Technology Plan Projects (SYG202124), Natural Science Foundation of the Jiangsu Higher Education Institutions of China (20KJA510003), and Priority Academic Program Development (PAPD) of Jiangsu Higher Education Institutions. Y.L. acknowledges the support by Singapore Ministry of Education (No. MOE2018-T2-2-189(S)). S.A.M. additionally acknowledges the Lee-Lucas Chair in Physics.

## Conflict of Interest

The authors declare no conflict of interest.

## Keywords

hot carriers, photodetection, surface plasmons

Received: December 15, 2021

Revised: February 18, 2022

Published online: March 18, 2022

- [1] J. Sung, G. Y. Lee, B. Lee, *Nanophotonics* **2019**, *8*, 1701.
- [2] H. Atwater, A. Polman, *Nat. Mater.* **2010**, *9*, 205.
- [3] K. Lin, H. Lin, B. Jia, *Nanophotonics* **2020**, *9*, 3135.
- [4] G. Li, B. P. Clarke, J. K. So, K. F. MacDonald, N. I. Zheludev, *Nat. Commun.* **2016**, *7*, 13705.
- [5] T. Xue, W. Liang, Y. Li, Y. Sun, Y. Xiang, Y. Zhang, Z. Dai, Y. Duo, L. Wu, K. Qi, B. N. Shivananju, L. Zhang, X. Cui, H. Zhang, Q. Bao, *Nat. Commun.* **2019**, *10*, 28.
- [6] A. Sobhani, M. W. Knight, Y. Wang, B. Zheng, N. S. King, L. V. Brown, Z. Fang, P. Nordlander, N. J. Halas, *Nat. Commun.* **2013**, *4*, 1643.
- [7] X. Li, N. P. Hylton, V. Giannini, K. H. Lee, A. M. Stefan, *Opt. Express* **2011**, *19*, A888.
- [8] C. Clavero, *Nat. Photonics* **2014**, *8*, 95.
- [9] J. G. Smith, J. A. Fauchaux, P. K. Jain, *Nano Today* **2015**, *10*, 67.
- [10] P. Narang, R. Sundararaman, H. A. Atwater, *Nanophotonics* **2016**, *5*, 96.
- [11] N. P. Hylton, X. F. Li, V. Giannini, K. H. Lee, N. J. Ekins-Daukes, J. Loo, D. Vercautse, P. Van Dorpe, H. Sodabanlu, M. Sugiyama, S. A. Maier, *Sci. Rep.* **2013**, *3*, 2874.
- [12] D. Lee, S. So, G. Hu, M. Kim, T. Badloe, H. Cho, J. Kim, H. Kim, C. Qiu, J. Rho, *eLight* **2022**, *2*, 1.
- [13] M. W. Knight, H. Sobhani, P. Nordlander, N. J. Halas, *Science* **2011**, *332*, 702.
- [14] P. Reineck, D. Brick, P. Mulvaney, U. Bach, *J. Phys. Chem. Lett.* **2016**, *7*, 4137.
- [15] J. Liu, J. Feng, J. Gui, T. Chen, M. Xu, H. Wang, H. Dong, H. Chen, X. Li, L. Wang, Z. Chen, Z. Yang, J. Liu, W. Hao, Y. Yao, L. Gu, Y. Weng, Y. Huang, X. Duan, J. Zhang, Y. Li, *Nano Energy* **2018**, *48*, 44.
- [16] Y. Zhu, H. Xu, P. Yu, Z. Wang, *Appl. Phys. Rev.* **2021**, *8*, 021305.
- [17] Y. Zhang, S. He, W. Guo, Y. Hu, J. Huang, J. R. Mulcahy, W. D. Wei, *Chem. Rev.* **2017**, *118*, 2927.
- [18] H. Tang, C. J. Chen, Z. Huang, J. Bright, G. Meng, R. Liu, N. Wu, *J. Chem. Phys.* **2020**, *152*, 220901.
- [19] A. Dorodnyy, Y. Salamin, P. Ma, J. V. Plestina, N. Lassaline, D. Mikulic, P. Romero-Gomez, A. F. i Morral, J. Leuthold, *IEEE J. Sel. Top. Quantum Electron.* **2018**, *24*, 4600313.
- [20] C. Scales, P. Berini, *IEEE J. Quantum Electron.* **2010**, *46*, 633.
- [21] Z. Wang, X. Wang, J. Liu, *ACS Photonics* **2018**, *5*, 3989.
- [22] H. Chalabi, D. Schoen, M. L. Brongersma, *Nano Lett.* **2014**, *14*, 1374.
- [23] J. C. J. Bart, *Plastics Additives: Advanced Industrial Analysis*, IOS Press, Amsterdam **2006**.
- [24] F. P. G. de Arquer, A. Mihi, G. Konstantatos, *ACS Photonics* **2015**, *2*, 950.
- [25] D. A. Bandurin, D. Svintsov, I. Gayduchenko, S. G. Xu, A. Principi, M. Moskotin, I. Tretyakov, D. Yagodkin, S. Zhukov, T. Taniguchi, K. Watanabe, I. V. Grigorieva, M. Polini, G. N. Goltsman, A. K. Geim, G. Fedorov, *Nat. Commun.* **2018**, *9*, 5392.
- [26] W. Guo, Z. Dong, Y. Xu, C. Liu, D. Wei, L. Zhang, X. Shi, C. Guo, H. Xu, G. Chen, L. Wang, K. Zhang, X. Chen, W. Lu, *Adv. Sci.* **2020**, *7*, 1902699.
- [27] L. Wang, J. Wang, C. Liu, H. Xu, A. Li, D. Wei, Y. Liu, G. Chen, X. Chen, W. Lu, *Adv. Funct. Mater.* **2019**, *29*, 1905057.
- [28] M. Moskovits, *Nat. Nanotechnol.* **2015**, *10*, 6.
- [29] M. Brongersma, N. J. Halas, P. Nordlander, *Nat. Nanotechnol.* **2015**, *10*, 25.
- [30] W. Li, J. G. Valentine, *Nanophotonics* **2017**, *6*, 177.
- [31] M. Casalino, G. Coppola, R. M. De La Rue, D. F. Logan, *Laser Photonics Rev.* **2016**, *10*, 895.
- [32] L. Shi, K. Chen, A. Zhai, G. Li, M. Fan, Y. Hao, F. Zhu, H. Zhang, Y. Cui, *Laser Photonics Rev.* **2021**, *21*, 2000401.
- [33] J. Fast, U. Aeberhard, S. P. Bremner, H. Linke, *Appl. Phys. Rev.* **2021**, *8*, 021309.
- [34] S. Kahmann, L. M. A. S. Kahmann, M. A. Loi, *J. Mater. Chem. C* **2019**, *7*, 2471.
- [35] H. Reddy, K. Wang, K. Zhaxylyk, L. Zhu, S. Yan, A. Vezzoli, S. J. Higgins, V. Gavini, A. Boltasseva, P. Reddy, V. M. Shalaev, E. Meyhofer, *Science* **2020**, *369*, 423.
- [36] M. Bernardi, J. Mustafa, J. B. Neaton, S. G. Louie, *Nat. Commun.* **2015**, *6*, 7044.
- [37] A. Manjavacas, J. G. Liu, V. Kulkarni, P. Nordlander, *ACS Nano* **2014**, *8*, 7630.
- [38] A. O. Govorov, H. Zhang, H. V. Demir, Y. K. Gun'ko, *Nano Today* **2014**, *9*, 85.
- [39] H. Zhu, H. Xie, Y. Yang, K. Wang, F. Zhao, W. Ye, W. Ni, *Nano Lett.* **2020**, *20*, 2423.
- [40] J. G. Liu, H. Zhang, S. Link, P. Nordlander, *ACS Photonics* **2017**, *5*, 2584.
- [41] R. Sundararaman, P. Narang, A. S. Jermyn, W. A. Goddard III, H. A. Atwater, *Nat. Commun.* **2014**, *5*, 5788.
- [42] A. M. Brown, R. Sundararaman, P. Narang, W. A. Goddard III, H. A. Atwater, *ACS Nano* **2016**, *10*, 957.
- [43] M. Lehr, B. Foerster, M. Schmitt, K. Krüger, C. Sönnichsen, G. Schönhense, H. J. Elmers, *Nano Lett.* **2017**, *17*, 6606.
- [44] A. M. Brown, R. Sundararaman, P. Narang, A. M. Schwartzberg, W. A. Goddard III, H. A. Atwater, *Phys. Rev. Lett.* **2017**, *118*, 087401.
- [45] O. Lozan, R. Sundararaman, B. Ea-Kim, J. M. Rampoux, P. Narang, S. Dilhaire, P. Lalanne, *Nat. Commun.* **2017**, *8*, 1656.

- [46] J. R. M. Saavedra, A. Asenjo-Garcia, F. J. García de Abajo, *ACS Photonics* **2016**, *3*, 1637.
- [47] O. Demichel, M. Petit, S. Viarbitskaya, R. Méjard, F. De Fornel, E. Hertz, F. Billard, A. Bouhelier, B. Cluzel, *ACS Photonics* **2016**, *3*, 791.
- [48] S. K. Cushing, *Nat. Photonics* **2017**, *11*, 748.
- [49] E. Blandre, D. Jalas, A. Yu Petrov, M. Eich, *ACS Photonics* **2018**, *5*, 3613.
- [50] K. Wu, J. Chen, J. R. McBride, T. Lian, *Science* **2015**, *349*, 632.
- [51] D. Li, X. Sun, H. Song, Z. Li, H. Jiang, Y. Chen, G. Miao, B. Shen, *Appl. Phys. Lett.* **2011**, *99*, 261102.
- [52] H. Lee, Y. K. Lee, E. Hwang, J. Y. Park, *J. Phys. Chem. C* **2014**, *118*, 5650.
- [53] C. Lee, Y. K. Lee, Y. Park, J. Y. Park, *ACS Photonics* **2018**, *5*, 3499.
- [54] C. Zhang, Q. Qian, L. Qin, X. Zhu, C. Wang, X. Li, *ACS Photonics* **2018**, *5*, 5079.
- [55] L. J. Krayer, E. M. Tennyson, M. S. Leite, J. N. Munday, *ACS Photonics* **2018**, *5*, 306.
- [56] W. Li, J. Valentine, *Nano Lett.* **2014**, *14*, 3510.
- [57] B. Desiatov, I. Goykhman, N. Mazurski, J. Shappir, J. B. Khurgin, A. Levy, *Optica* **2015**, *2*, 335.
- [58] K. T. Lin, H. L. Chen, Y. S. Lai, C. C. Yu, *Nat. Commun.* **2014**, *5*, 3288.
- [59] M. Tanzid, A. Ahmadvand, R. Zhang, B. Cerjan, A. Sobhani, S. Yazdi, P. Nordlander, N. J. Halas, *ACS Photonics* **2018**, *5*, 3472.
- [60] L. Wen, Y. Chen, W. Liu, Q. Su, J. Grant, Z. Qi, Q. Wang, Q. Chen, *Laser Photonics Rev.* **2017**, *11*, 1700059.
- [61] L. Wen, Y. Chen, L. Liang, Q. Chen, *ACS Photonics* **2018**, *5*, 581.
- [62] T. Gong, J. N. Munday, *Nano Lett.* **2015**, *15*, 147.
- [63] C. Zhang, K. Wu, Y. Zhan, V. Giannini, X. Li, *Nanoscale* **2016**, *8*, 10323.
- [64] C. Zhang, K. Wu, V. Giannini, X. Li, *ACS Nano* **2017**, *11*, 1719.
- [65] Z. Wang, J. K. Clark, Y. L. Ho, J. J. Delaunay, *Nanoscale* **2019**, *11*, 17407.
- [66] S. Ishii, S. L. Shinde, W. Jevasuwan, N. Fukata, T. Nagao, *ACS Photonics* **2016**, *3*, 1552.
- [67] C. Zhang, T. Liu, L. Li, S. Wu, C. Wang, X. Li, *IEEE J. Sel. Top. Quantum Electron.* **2021**, *28*, 3800109.
- [68] S. L. Shinde, S. Ishii, T. Nagao, *ACS Appl. Mater. Interfaces* **2019**, *11*, 21965.
- [69] C. Zhang, G. Cao, S. Wu, W. Shao, V. Giannini, S. A. Maier, X. Li, *Nano Energy* **2019**, *55*, 164.
- [70] M. Sakhdari, M. Hajizadegan, M. Farhat, P. Y. Chen, *Nano Energy* **2016**, *26*, 371.
- [71] J. Hou, H. Zhu, J. C. Reed, F. Yi, E. Cubukcu, D. A. Bonnell, *Appl. Phys. Lett.* **2017**, *110*, 043103.
- [72] T. Y. Lin, K. T. Lin, C. C. Lin, Y. W. Lee, L. T. Shiu, W. Y. Chen, H. L. Chen, *Mater. Horiz.* **2016**, *6*, 1156.
- [73] T. Gong, J. N. Munday, *Opt. Mater. Express* **2015**, *5*, 2501.
- [74] T. P. White, K. R. Catchpole, *Appl. Phys. Lett.* **2012**, *101*, 073905.
- [75] S. Zhao, Y. Yin, J. Peng, Y. Wu, G. G. Andersson, F. J. Beck, *Adv. Opt. Mater.* **2020**, *9*, 2001121.
- [76] M. W. Knight, Y. Wang, A. S. Urban, A. Sobhani, N. J. Halas, *Nano Lett.* **2013**, *13*, 1687.
- [77] I. Goykhman, B. Desiatov, J. Khurgin, J. Shappir, U. Levy, *Opt. Express* **2012**, *20*, 28594.
- [78] M. Grajower, U. Levy, J. B. Khurgin, *ACS Photonics* **2018**, *5*, 4030.
- [79] N. A. Günsken, A. Lauri, Y. Li, T. Matsui, S. A. Maier, *ACS Photonics* **2019**, *6*, 953.
- [80] J. Xiong, S. Wu, *eLight* **2021**, *1*, 3.
- [81] S. O. Kasap, *Principles of Electronic Materials and Devices*, McGraw-Hill, New York **2006**.
- [82] S. Ishii, S. L. Shinde, T. Nagao, *Adv. Opt. Mater.* **2019**, *7*, 1800603.
- [83] L. V. Besteiro, X. T. Kong, Z. Wang, G. V. Hartland, A. O. Govorov, *ACS Photonics* **2017**, *4*, 2759.
- [84] J. Aizpurua, J. Baumberg, A. Boltasseva, P. Christopher, E. Cortes, S. B. Cronin, B. K. Dadhich, B. de Nijs, *Faraday Discuss.* **2019**, *214*, 365.
- [85] G. V. Hartland, L. V. Besteiro, P. Johns, A. O. Govorov, *ACS Energy Lett.* **2017**, *2*, 1641.
- [86] M. Kumar, N. Umezawa, S. Ishii, T. Nagao, *ACS Photonics* **2016**, *3*, 43.
- [87] B. Doiron, M. Mota, M. P. Wells, R. Bower, A. Mihai, Y. Li, L. F. Cohen, N. M. Alford, P. K. Petrov, R. F. Oulton, S. A. Maier, *ACS Photonics* **2019**, *6*, 240.
- [88] Q. Sun, C. Zhang, W. Shao, X. Li, *ACS Omega* **2019**, *4*, 6020.
- [89] M. Alavirad, A. Olivieri, L. Roy, P. Berini, *Opt. Express* **2016**, *24*, 22544.
- [90] K. F. Mak, J. Shan, *Nat. Photonics* **2016**, *10*, 216.
- [91] F. Xia, H. Wang, D. Xiao, M. Dubey, A. Ramasubramaniam, *Nat. Photonics* **2014**, *8*, 899.
- [92] A. B. Khanikaev, G. Shvets, *Nat. Photonics* **2017**, *11*, 763.
- [93] Y. Tang, K. F. Mak, *Nat. Nanotechnol.* **2017**, *12*, 1121.
- [94] H. Shan, Y. Yu, X. Wang, Y. Luo, S. Zu, B. Du, T. Han, B. Li, Y. Li, J. Wu, F. Lin, K. Shi, B. K. Tay, L. Z. X. Zhu, Z. Fang, *Light: Sci. Appl.* **2019**, *8*, 9.
- [95] I. Goykhman, U. Sassi, B. Desiatov, N. Mazurski, S. Milana, D. de Fazio, A. Eiden, J. Khurgin, J. Shappir, U. Levy, A. C. Ferrari, *Nano Lett.* **2016**, *16*, 3005.
- [96] Y. Park, J. Choi, C. Lee, A. N. Cho, J. Y. Park, *Nano Lett.* **2019**, *19*, 5489.
- [97] M. Grajower, B. Desiatov, N. Mazurski, J. Shappir, J. B. Khurgin, U. Levy, *ACS Photonics* **2017**, *4*, 1015.
- [98] A. Pescaglini, A. Martín, D. Cammi, G. Juska, C. Ronning, E. Pelucchi, D. Iacopino, *Nano Lett.* **2014**, *14*, 6202.
- [99] Y. Yu, Z. Ji, S. Zu, B. Du, Y. Kang, Z. Li, Z. Zhou, K. Shi, Z. Fang, *Adv. Funct. Mater.* **2016**, *26*, 6394.
- [100] A. Giugni, B. Torre, A. Toma, M. Malerba, A. Alabastri, R. Proietti Zaccaria, M. I. Stockman, E. Di Fabrizio, *Nat. Nanotechnol.* **2013**, *8*, 845.
- [101] W. Li, Z. J. Coppens, L. V. Besteiro, W. Wang, A. O. Govorov, J. Valentine, *Nat. Commun.* **2015**, *6*, 8379.
- [102] L. Wen, L. Liang, X. Yang, Z. Liu, Q. Chen, *ACS Nano* **2019**, *13*, 6963.
- [103] F. Wang, N. A. Melosh, *Nat. Commun.* **2013**, *4*, 1711.
- [104] X. D. Gao, G. T. Fei, Y. Zhang, L. D., Zhang, Z. M. Hu, *Adv. Funct. Mater.* **2018**, *28*, 1802288.
- [105] M. Taghinejad, H. Taghinejad, Z. Xu, T. Liu, S. P. Rodrigues, K. Lee, T. Lian, A. Adibi, W. Cai, *Adv. Mater.* **2018**, *30*, 1704915.
- [106] S. Simoncelli, Y. Li, E. Cortés, S. A. Maier, *ACS Nano* **2018**, *12*, 2184.
- [107] H. Shokri Kojori, J. H. Yun, Y. Paik, J. Kim, W. A. Anderson, S. J. Kim, *Nano Lett.* **2016**, *16*, 250.
- [108] Y. L. Ho, Y. H. Tai, J. K. Clark, Z. Wang, P. K. Wei, J. J. Delaunay, *ACS Photonics* **2018**, *5*, 2617.
- [109] Y. L. Ho, L. C. Huang, J. J. Delaunay, *Nano Lett.* **2016**, *16*, 3094.
- [110] S. Ishii, S. Inoue, R. Ueda, A. Otomo, *ACS Photonics* **2014**, *1*, 1089.
- [111] L. Zhou, C. Zhang, L. Li, T. Liu, K. Li, S. Wu, X. Li, *Opt. Express* **2021**, *29*, 15505.
- [112] B. Feng, J. Zhu, B. Lu, F. Liu, Y. Chen, *ACS Nano* **2019**, *13*, 8433.
- [113] C. Liu, J. Guo, L. Yu, J. Li, M. Zhang, H. Li, Y. Shi, D. Dai, *Light: Sci. Appl.* **2021**, *10*, 123.
- [114] A. Habib, F. Florio, R. Sundararaman, *J. Opt.* **2018**, *20*, 064001.
- [115] R. Lin, W. Zheng, D. Zhang, Z. Zhang, Q. Liao, L. Yang, F. Huang, *ACS Appl. Mater. Interfaces* **2018**, *10*, 22419.
- [116] A. Ahmadvand, R. Sinha, P. K. Vabbina, M. Karabiyik, S. Kaya, N. Pala, *Opt. Express* **2016**, *24*, 13665.
- [117] T. Gong, J. N. Munday, *Appl. Phys. Lett.* **2011**, *110*, 021117.
- [118] F. Wang, N. A. Melosh, *Nano Lett.* **2011**, *11*, 5426.
- [119] H. Elabd, W. F. Kosonocky, *RCA Rev.* **1982**, *43*, 569.

- [120] L. J. Kraye, K. J. Palm, C. Gong, A. Torres, J. N. Munday, *ACS Photonics* **2020**, *7*, 1689.
- [121] M. Casalino, L. Sirleto, M. Iodice, N. Saffioti, M. Gioffre, I. Rendina, G. Coppola, *Appl. Phys. Lett.* **2010**, *96*, 241112.
- [122] Z. Yang, K. Du, H. Wang, F. Lu, Y. Pang, J. Wang, X. Gan, W. Zhang, T. Mei, S. J. Chua, *Nanotechnology* **2019**, *30*, 075204.
- [123] W. Wang, A. Klots, D. Prasai, Y. Yang, K. I. Bolotin, J. Valentine, *Nano Lett.* **2015**, *15*, 7440.
- [124] I. Goykhman, B. Desiatov, J. Khurgin, J. Shappir, U. Levy, *Nano Lett.* **2011**, *11*, 2219.
- [125] A. Akbari, P. Berini, *Appl. Phys. Lett.* **2009**, *95*, 021104.
- [126] A. Akbari, R. N. Tait, P. Berini, *Opt. Express* **2010**, *18*, 8505.
- [127] S. Muehlbrandt, A. Melikyan, T. Harter, K. Khnlé, M. Kohl, *Optica* **2016**, *3*, 741.



**Cheng Zhang** received B.Eng. (2013) and Ph.D. (2018) degrees from Soochow University, China. He is currently working as an associate professor in the School of Optoelectronic Science and Engineering, Soochow University, China. His research interests include the high-performance hot-carrier photodetection and applications. He has published over 10 first/corresponding authored papers in journals including ACS Nano, Nano Energy, Nanoscale, Applied Physics Letters, Optics Letters, Optics Express, etc.



**Yu Luo** is received the Ph.D in physics from Imperial College London in 2012 and joined Nanyang Technological University in 2015, where he is currently an associate professor. Prof. Luo's research interests focus on the design of metamaterials and plasmonics from fundamental aspects to various practical applications. His recent work has resulted in a number of high-impact journal publications in Science, Nature Physics, PNAS, and PRL and has been highlighted by many scientific magazines and public media, including Nature Photonics, Nature Physics, Physics World, Phys.org, BBC News, Guardian, etc.



**Stefan A. Maier** holds the Chair in Hybrid Nanosystems at Ludwig-Maximilians-Universität München, and the Lee-Lucas Chair in Physics at Imperial College London. He is a fellow of the Optical Society of America and of the Institute of Physics. His current research focuses on plasmonics, hot-electron chemistry, and dielectric nanophotonics.



**Xiaofeng Li** received B.Eng. and Ph.D. degrees from Southwest Jiaotong University, China, in 2002 and 2007, respectively. From 2007 to 2011, he has been working in Nanyang Technological University and Imperial College London. He began to work in Soochow University as a professor since 2012. He is now the dean of School of Optoelectronic Science and Engineering, Soochow University. His interests include photovoltaics, photodetectors, nanophotonic systems/devices, etc. He has authored over 160 journal papers and presented over 50 invited talks. He had been serving as an associate editor of Applied Optics and IEEE Photonics journal.